Environmental Science & Technology

pubs.acs.org/est

Article

Cadmium Isotope Fractionation during Adsorption onto Edge Sites and Vacancies in Phyllomanganate

Hui Yin,*,& Xinran Yan, Chuanwei Zhu,* Kideok D. Kwon,& Xueyuan Gu, Wei Zhao, Bruno Lanson, Wei Li, Jingyuan Ma, Yan Li, Jiangshan Li, Guohong Qiu, Xionghan Feng, Wenfeng Tan, Hanjie Wen, Qiaoyun Huang, and Fan Liu

Cite This: *Environ. Sci. Technol.* 2024, 58, 13498−13508

ABSTRACT: Cadmium (Cd) geochemical behavior is strongly influenced by its adsorption onto natural phyllomanganates, which contain both layer edge sites and vacancies; however, Cd isotope fractionation mechanisms at these sites have not yet been addressed. In the present work, Cd isotope fractionation during adsorption onto hexagonal (containing both types of sites) and triclinic birnessite (almost only edge sites) was investigated using a combination of batch adsorption experiments, extended X-ray absorption fine structure (EXAFS) spectroscopy, surface complexation modeling, and density functional theory (DFT) calculations. Light Cd isotopes are preferentially enriched on solid surfaces, and the isotope fractionation induced by Cd^{2+} adsorption on edge sites ($\Delta^{114/110}Cd_{edge\text{-}solution}$ = −1.54 ± 0.11‰) is smaller than that on vacancies ($\Delta^{114/110}Cd_{vacancy\text{-}solution}$ = −0.71 ± 0.21‰), independent of surface coverage or pH. Both Cd K-edge EXAFS and DFT results indicate the formation of double corner-sharing complexes on layer edge sites and mainly triple cornering-sharing complexes on vacancies. The distortion of both complexes results in the negative isotope fractionation onto the solids, and the slightly longer first Cd−O distances and a smaller number of nearest Mn atoms around Cd at edge sites probably account for the larger fractionation magnitude compared to that of vacancies. These results provide deep insights into Cd isotope fractionation mechanisms during interactions with phyllomanganates.

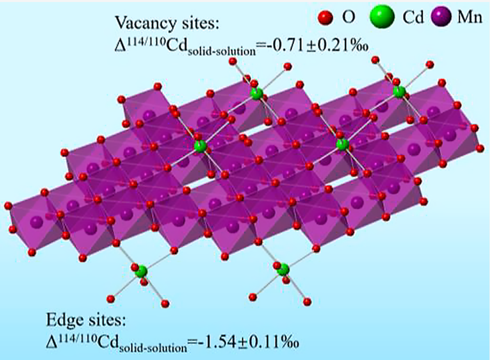

KEYWORDS: *phyllomanganate, cadmium adsorption, isotope fractionation, vacancies, edge sites*

1. INTRODUCTION

The increase in cadmium (Cd) contamination has greatly enhanced the study of its sources and behavior in the environment owing to its toxicity and carcinogenicity for living organisms including humans.[1] Anthropogenic activities, such as mining, smelting, chemical industries, and fertilizer use result in the release of Cd into soils and aquatic and atmospheric environments, which is significantly larger than that from natural weathering.[2] Source identification is of prime importance for the prediction and remediation of Cd pollution, and Cd isotopic signature may bring key information to deciphering Cd biogeochemical cycling and fingerprinting Cd sources and fates.[3−6] Notably, biogeochemical reactions, such as adsorption and desorption,[7] precipitation and dissolution,[8] evaporation and condensation,[9] weathering,[10] and biological uptake,[11] may induce isotope fractionation and modify Cd isotopic signature. Therefore, the identification of isotope fractionation during these geochemical processes at environmentally relevant interfaces is key to constraining Cd isotopic signatures in nature.

One of the important interface reactions affecting Cd isotope fractionation is adsorption to manganese (Mn) dioxides. Mn dioxides occur naturally and widely as lamellar compounds (phyllomanganate) in aquatic systems, soils, and marine sediments and play significant roles in controlling the geochemical cycling and fate of heavy metals due to their small particle sizes, structural defects, and negatively charged surfaces.[12−17] Layers of the phyllomanganate birnessite are composed of edge-sharing $Mn(IV)O_6$ and $Mn(III)O_6$ octahedra and vacancies. Since $Mn(III)O_6$ octahedra are distorted by the Jahn−Teller effect, different concentrations and spatial distributions of Mn(III) in the birnessite layers result in the layer symmetry being either hexagonal or orthogonal. Birnessite with orthogonal layer symmetry (triclinic birnessite, TBir) contains almost no or only a small amount of layer vacancy but high amounts (∼33%) of layer Mn(III) aligned in rows[18−22] (Figure 1a). In contrast, birnessite with hexagonal layer symmetry (hexagonal birnes-

Received: April 17, 2024
Revised: July 10, 2024
Accepted: July 11, 2024
Published: July 18, 2024

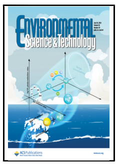

https://doi.org/10.1021/acs.est.4c03808
Environ. Sci. Technol. 2024, 58, 13498−13508

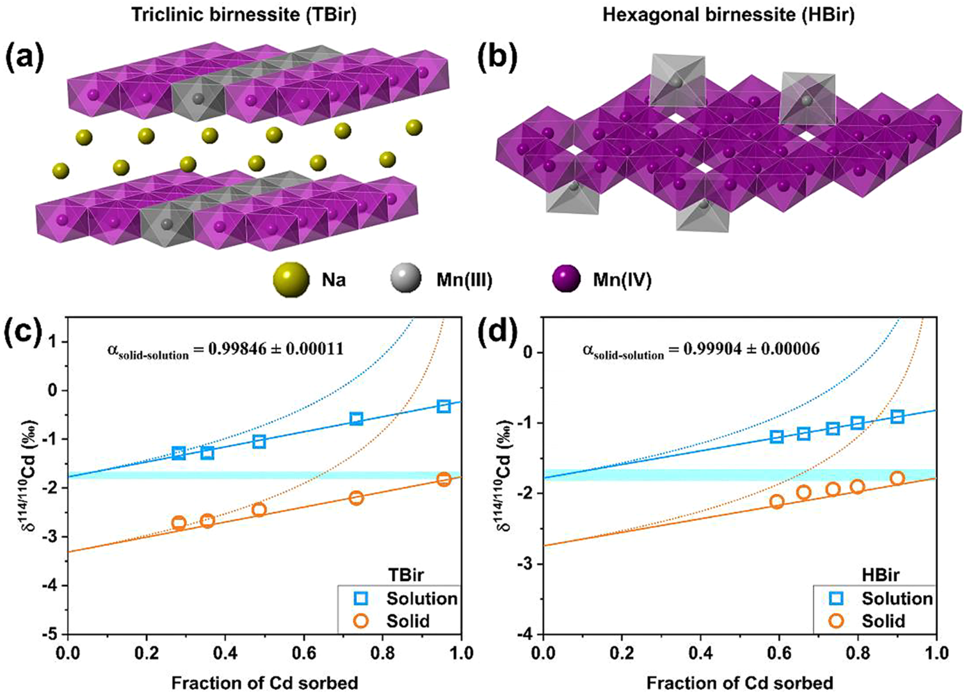

Figure 1. Idealized structures of triclinic birnessite (a) and hexagonal birnessite (b) and Cd isotopic compositions of the solution and solid phases as a function of the adsorbed Cd fraction (*f*) during adsorption onto triclinic birnessite TBir (c) and hexagonal birnessite HBir (d). The $\delta^{114/110}$Cd of the bulk solution is −1.74 ± 0.08‰. In panels c and d, the solid and dotted lines are the best fittings based on the equilibrium and Rayleigh models, respectively.

site, HBir) contains a relatively high concentration of vacancies (10−20%) but few or no layer Mn(III) (Figure 1b). The presence of vacancies and/or Mn(III) in the birnessite layers and the unsaturated O atoms at the layer edges result in a large negative layer charge.[23,24] This leads to a high reactivity of birnessite toward heavy metal adsorption. Previous studies using powder X-ray diffraction, extended X-ray absorption fine structure (EXAFS), differential pair distribution function (d-PDF), and density functional theory (DFT) analyses reported that heavy metals (such as Pb, Co, Cu, Ni, and Zn) are adsorbed onto hexagonal birnessite mainly as triple-corner-sharing (TCS) surface complexes on vacancies, triple-edge-sharing (TES) complexes above tridentate cavities on birnessite basal planes, and/or double-corner sharing (DCS) and double-edge sharing (DES) complexes on lateral edge surfaces.[24−34] By contrast, only a few studies have investigated molecular mechanisms of Cd adsorption on birnessites. The d-PDF analysis of Cd adsorption onto poorly crystalline hexagonal birnessite demonstrated the major role of layer vacancies.[35] More precisely, Cd K-edge EXAFS analysis showed that during adsorption onto hexagonal birnessite with uncapped vacancies, Cd was mainly adsorbed as TCS complexes on vacancies with a minor amount of DCS complexes on edge sites, whereas Cd was predominantly bound onto edge sites as DCS and DES complexes on Mn(III)-rich hexagonal birnessite.[36]

Adsorption of heavy metals onto solid surfaces can induce isotope fractionation.[37−41] Previous studies have demonstrated that light Cd isotopes are preferentially adsorbed onto soil active minerals (e.g., Fe/Mn/Al (hydr)oxides, clay minerals, calcite, and quartz).[7,42−44] However, fractionation mechanisms during such interface reactions are not clearly constrained. Our previous study on Cd isotope fractionation during adsorption onto Fe (hydr)oxides revealed that the isotope offsets were independent of reaction conditions, such as ionic strength, initial Cd concentration, and pH, as well as mineral type, but were attributed only to the strong distortion of CdO_6 octahedra formed at mineral surfaces.[7] Similarly, Cd adsorbed onto calcite surfaces was also reported to form distorted octahedra and to induce isotope fractionation independent of reaction conditions, but the presence of inorganic ligands (e.g., phosphate) reduced the fractionation magnitude.[44] The sole study on Cd isotope fractionation during adsorption onto Mn dioxides demonstrated that Cd isotope fractionation during adsorption onto hexagonal birnessite was dependent on ionic strength and reaction time.[40] The fractionation magnitude was larger in synthetic seawater than that at low ionic strength, probably because of the abundance of isotopically light chloro-complexes (e.g., $CdCl^+$) under the former conditions.[40] Although fractionation reached a reversible equilibrium at low ionic strength, fractionation magnitude decreased gradually with time in synthetic seawater; after 1, 24, and 912 h reaction times, the fractionations ($\Delta^{114/110}Cd_{solid\text{-}solution}$) were −0.8, −0.4, and −0.2‰. Alterations in the mineral structure and crystallinity and in the molecular mechanisms of Cd binding with time were hypothesized as possible explanations.[40] This may also suggest a change in the relative proportions of Cd^{2+} binding to vacancies and edge sites. However, no data coupling the Cd isotope fractionation behaviors with these distinct active sites in the birnessite structure were available to support the hypothesis.

The present study thus aimed at determining Cd isotope fractionation during adsorption onto birnessite vacancy sites and layer edge sites. Cd isotope fractionation during adsorption onto triclinic birnessite and hexagonal birnessite over pH 4−8 was investigated first. Then, Cd K-edge EXAFS and DFT calculations were combined to investigate the mechanisms of binding of Cd to birnessite surface active

https://doi.org/10.1021/acs.est.4c03808

sites, and surface complexation modeling was used to determine the relative proportions of Cd^{2+} binding to birnessite vacancies and edge sites. Finally, the Cd isotope fractionation onto birnessite vacancies was determined by using triclinic birnessite as an end member for layer edge sites, and the Cd isotope fractionation on these two types of active sites on birnessite was coupled to the Cd^{2+} binding mechanisms at the molecular level. These results greatly enhance our understanding of Cd isotope fractionation and underlying mechanisms induced by its sorption to phyllomanganates and the application of Cd isotopes as tracers in natural environments.

2. MATERIALS AND METHODS

2.1. Synthesis and Properties of Hexagonal and Triclinic Birnessite Samples. All reagents were used as received, and detailed information is provided in the Supporting Information in Text S1. For triclinic birnessite (TBir) synthesis, 250 mL of 5.5 M NaOH solution was refrigerated at 4 °C for 5 h and then quickly added to 200 mL of 0.5 M $MnCl_2$ solution in a 500 mL Erlenmeyer flask. Immediately, high-purity oxygen gas (99.999%) was flowed in the obtained suspension at 2 $L\cdot min^{-1}$ for 5 h under vigorous stirring.[45] For hexagonal birnessite (HBir) synthesis, 300 mL of a 0.667 M $KMnO_4$ solution in a 500 mL Erlenmeyer flask was heated to 100 °C in an oil bath with a glass condenser. Then, 45 mL of a 6 M HCl solution was added at a constant rate of 0.7 $mL\cdot min^{-1}$, followed by a further 30 min of reaction. The resulting suspension was cooled naturally at room temperature and then aged at 60 °C for 12 h.[46] After synthesis, the solids were obtained through centrifugation, washed until the conductivity was below 20 $\mu S\cdot cm^{-1}$, freeze-dried, ground, sieved, and then stored at 4 °C.

Mineral phases and morphologies were identified by powder X-ray diffraction (XRD) and scanning electron microscopy (SEM) (Figure S1). For chemical composition analysis, 0.01 g of solid and 0.1 g of hydroxylamine hydrochloride were accurately weighed and diluted in 250 mL of deionized water. The contents of K, Na, and Mn in solution were determined by a flame atomic absorption spectrometer (FAAS, Agilent Technologies 200 Series AA). The Mn and K contents are 53.50 ± 0.06 and 8.72 ± 0.07% for HBir, and the Mn and Na contents are 57.22 ± 0.40 and 5.64 ± 0.00% for TBir. Points of zero charge (PZCs) of HBir and TBir were determined to be ∼0.9 and ∼3.4, respectively, by a Zeta potential method[47] (Figure S2), and their N_2−BET specific surface areas are 26.33 ± 0.25 and 25.92 ± 0.21 $m^2\cdot g^{-1}$. Mn average oxidation states of HBir and TBir were determined to be 4.02 ± 0.01 and 3.67 ± 0.02, respectively, by potentiometric titration.[34]

The microstructural characteristics of HBir, including vacancy content and crystallite size, were determined by a specific trial-and-error method[34,48] (Text S2, Figures S3 and S4, and Table S1). The structural formula was determined to be $K_{0.22}(Mn_{0.94}\square_{0.06})O_2\cdot 0.33H_2O$ (□ denotes vacancy). Typically, an orthogonal setting was used for the unit cell with a = 4.922 Å, b = 2.842 Å, and c^* = 7.20 Å. The diameter of disk-like coherent scattering domains (CSD) in the ab plane was calculated to be 180 or 160 Å from (20,11) or (02,31) diffraction band modeling, respectively, while that along the c* axis was determined to be 79 ± 2 Å by the Scherrer formula.[49]

2.2. Cd^{2+} Adsorption Experiments. Two series of adsorption experiments were conducted, including kinetic adsorption experiments with different reaction times (0−360 h for TBir and 0−720 h for HBir) at pH 6 and adsorption edge experiments varying from pH 4 to 8 for 72 h. Prior to the addition of the Cd^{2+} solution, solids were equilibrated at pH 6 ± 0.05 in 0.1 M $NaNO_3$ solution for 24 h with mineral concentrations of 0.5 $g\cdot L^{-1}$ for TBir and 0.1 $g\cdot L^{-1}$ for HBir. To initiate the adsorption reaction, volumes of Cd^{2+} stock solution were added to mineral suspensions to obtain the concentrations of 133.4 μM for TBir and 266.9 and 177.9 μM for HBir in kinetic and pH edge experiments, respectively. These Cd^{2+} concentrations were selected to prevent Cd^{2+} precipitation and investigate the relationships between adsorption and isotope fractionation over a wide range of adsorption proportions. The suspension pH was adjusted and maintained by adding 1 M HNO_3 or 1 M NaOH.

At the end of the reactions, mineral suspensions were filtered through 0.2 μm cellulose membranes to separate the solid and the solution phases. The obtained solid was then sealed with Kapton tape and stored at 4 °C within 24 h prior to Cd K-edge-extended X-ray absorption fine structure (EXAFS) analysis. The Cd^{2+} concentrations in the filtrates were determined using FAAS with a detection limit of 6.77 $\mu g\cdot L^{-1}$ and an uncertainty of 0.3%. Control experiments were carried out with no Cd^{2+} added to the mineral suspensions to exclude potential Cd^{2+} contamination. Duplicate experiments were carried out to ensure reproducibility.

To investigate the possible mineral transformation of TBir under acidic conditions used for Cd^{2+} adsorption, a 0.5 $g\cdot L^{-1}$ TBir suspension was processed as described above for adsorption experiments conducted at pH4 but without Cd^{2+}. At the end of the reaction, the suspension was centrifugated; the solid obtained (TBir_pH4_72h) was characterized using powder XRD analysis, and the supernatant was analyzed by FAAS for dissolved Mn concentration.

2.3. Cd Isotope Measurements. Prior to isotope analysis, solids with adsorbed Cd were transferred to 25 mL acid-cleaned Teflon vials and dissolved by adding 10 mL of warm 3 M HCl solution.[40] Then, an aliquot of each sample containing ∼600 ng Cd was mixed with a ^{111}Cd-^{110}Cd double-spike solution containing an equal mass of Cd and subjected to chemical separation and purification as described previously.[7,50,51] The total Cd recovery was >95% for all samples. Cadmium isotopic ratio measurements were performed using a Thermo Scientific Neptune plus multi-collector inductively coupled plasma mass spectrometer (MC−ICP−MS) at the State Key Laboratory of Ore Deposit Geochemistry, Institute of Geochemistry, CAS. The double spike method allowed for correcting the mass bias. Measurement details were described previously.[7]

Double spike data reduction was performed offline to calculate Cd isotopic compositions of the samples and standards using a MATLAB-based script.[7,52,53] These isotopic compositions were reported relative to the NIST SRM 3108 Cd standard according to eq 1:

$$\delta^{114/110}\mathrm{Cd} = \left[\frac{\left(^{114}\mathrm{Cd}/^{110}\mathrm{Cd}\right)_{\mathrm{sample}}}{\left(^{114}\mathrm{Cd}/^{110}\mathrm{Cd}\right)_{\mathrm{NISTSRM3108}}} - 1\right] \times 1000 \tag{1}$$

In this study, $\delta^{114/110}Cd$ values of the secondary reference standards were −1.76 ± 0.06 ‰ (2SD; n = 4) for JMC Cd and −1.27 ± 0.05 ‰ (2SD; n = 4) for Spex Cd, consistent with previous results.[7,52,54] The long-term reproducibility of this method was better than ±0.08‰ (2SD; $N = 20$) for $\delta^{114/110}$Cd. Cd isotopic fractionation ($\Delta^{114/110}\mathrm{Cd}_{\text{soild-solution}}$) between the adsorbed and aqueous phases is defined as eq 2:

$$\Delta^{114/110}\mathrm{Cd}_{\text{solid}-\text{solution}} = \delta^{114/110}\mathrm{Cd}_{\text{solid}} - \delta^{114/110}\mathrm{Cd}_{\text{solution}} \quad (2)$$

2.4. EXAFS Data Collection and Analysis. The Cd K-edge EXAFS spectra of Cd-adsorbed Mn dioxides, Cd hydroxide, and aqueous $Cd(NO_3)_2$ standards were collected in fluorescence or transmission mode at the Shanghai Synchrotron Radiation Facility on a BL14W1 beamline with a pair of Si(111) monochromators. Energy calibration (E_0 = 25,529 eV) was conducted using a silver foil. IFEFFIT software was used for data processing.[55] The parameters used for background removal were as follows: E_0 = 26,715 eV, k-weight = 2, and Rbkg = 1.0. Structural parameters, including the interatomic distance (R), coordination number (CN), and Debye−Waller factor (σ^2), were obtained by fitting the experimental k^2-weighted spectra to the standard equation[56] over a k range of 2.5−9.8 Å^{-1} and an R range of 1−4 Å. An amplitude reduction factor ($S_0{}^2$) of 0.95 was adopted from previous studies.[7,36] During the first Cd−O shell fitting, a Gaussian or a non-Gaussian distribution model was assumed, with a third cumulant in the latter to interpret the asymmetry of the $[CdO_6]$ octahedron.[57]

2.5. Modeling of Cd^{2+} Adsorption on Hexagonal Birnessite Edge Sites and Vacancies. To determine the relative proportions of Cd^{2+} adsorbed to vacancy and edge sites of hexagonal birnessite, surface complexation modeling (SCM) of the Cd^{2+} adsorption envelope at pH 4−8 was conducted as described previously.[58] Hexagonal birnessite surfaces were divided into internal surfaces (three $\equiv Mn_2O^{-2/3}$ sites around each vacancy) and external edge surfaces ($\equiv Mn_2O^{-2/3}$ and $\equiv MnOH^{-1/3}$ sites), and a two-site model was used to describe mineral surface heterogeneity. The constant capacity model (CCM) was adopted to describe surface electrostatic effects on internal surfaces, while charge-distribution multisite ion complexation (CD-MUSIC) combined with the triple-layer model (TLM) was used to describe electrostatic effects on edge sites. The software ECOSAT 4.9[59] and the fitting program FIT[60] were used to fit the data.

2.6. DFT Geometry Optimization. An edge-sharing Mn octahedral nanodisk with a diameter of approximately 1.5 nm (i.e., $Mn_{19}O_{54}H_{30}$) was used as a model for birnessite (Figure S5). A Mn(IV) vacancy was created in the nanodisk model by removing one Mn octahedron, and two Cd cations were placed above and below the vacancy site to model TCS surface complexes. Each Cd was additionally coordinated to three H_2O molecules to ensure its octahedral coordination. TES surface complexes were created by placing a Cd cation on top of a tridentate cavity defined by three Mn octahedra representing surface complexes formed on a vacancy-free birnessite basal surface. For the DCS surface complex, Cd was initially coordinated to two singly coordinated O atoms of the lateral edge and four H_2O molecules. For the DES surface complexes, $Cd{\cdot}3H_2O$ was initially coordinated to one doubly coordinated O (DESI) or one triply coordinated O (DESII) and two singly coordinated O atoms on the lateral edge.

All DFT calculations were performed using CASTEP code[61] under the spin-polarized generalized gradient approximation, with the Perdew−Burke−Ernzerhof (PBE) functional.[62] The valence electron states of the Mn, Cd, O, and H ultrasoft pseudopotentials[63] were 3 $s^2 3p^6 3d^5 4s^2$, $4d^{10} 5s^2$, 2 $s^2 2p^4$, and $1s^1$, respectively. The kinetic energy cutoff was 500 eV. The k-point grid for the first Brillouin zone[64] was 1 × 1 × 1 for vernadite models. The k-point grids for CdO, $Cd(OH)_2$, and $Cd(NO_3)_2$ were 6 × 6 × 6, 8 × 8 × 6, and 4 × 2 × 4, respectively. The calculated atomic forces converged to less than 0.01 eV/Å. The magnetic ordering among edge-sharing Mn octahedra was ferromagnetic in the birnessite models. Geometry optimization was performed until the following conditions were met: total energy ≤0.000005 eV, atomic forces ≤0.05 eV/Å, stress ≤0.03 GPa, and atomic displacement ≤0.0005 Å. The crystal structures were rendered using VESTA software.[65]

3. RESULTS AND DISCUSSION

3.1. Cd Isotope Fractionation Behaviors during Adsorption onto Birnessites. At pH 6, surface coverages of Cd^{2+} adsorbed to Mn dioxides rapidly increase to reach a plateau (Figure S6a,b). After 72 h of reaction, the percentages of Cd^{2+} adsorbed are 57.0 ± 1.1% for TBir and 64.2 ± 0.3% for HBir, resulting in surface coverages of 5.87 ± 0.11 and 65.02 ± 0.32 μmol·m^{-2}, respectively (Table S2). These results suggest that the adsorption equilibrium between solids and solutions was reached after 72 h, and pH edge experiments were thus performed for 72 h. The density of Cd^{2+} sorbed to Mn dioxides increases as the pH increases from 4 to 8 (Figure S6c,d). As the pH increases, the surface coverage of Cd^{2+} increases from 3.00 ± 0.10 to 9.83 ± 0.01 μmol m^{-2} for TBir and from 46.39 ± 0.12 to 62.36 ± 0.03 μmol·m^{-2} for HBir (Table S3). Correspondingly, the percentages of Cd^{2+} adsorbed vary from 29.1 ± 1.0 to 95.5 ± 0.1 and 68.7 ± 1.2 to 92.3 ± 0.3%. These results indicate that Cd^{2+} adsorption to HBir is enhanced compared to TBir owing to the lower point of zero charge (PZC) (Figure S2) and the presence of highly undersaturated layer O atoms in HBir owing to layer vacancies.[66,67]

For TBir the isotopic composition ($\delta^{114/110}$Cd) of aqueous Cd^{2+} rapidly increases at the initial stage of the reaction and then reaches isotopic equilibrium (Figure S7 and Table S4). In detail, the $\delta^{114/110}$Cd value of the aqueous phases increases from −1.49 ± 0.08 to −1.10 ± 0.08 ‰ for TBir as the reaction time increases from 1 to 72 h and then remains essentially constant. Therefore, Cd adsorbed on Mn dioxides reaches isotopic equilibrium within 72 h. Compared to the $\delta^{114/110}$Cd value of the Cd^{2+} bulk solution (−1.74 ± 0.08‰), heavy Cd isotopes are preferentially enriched in the aqueous phase.

The $\delta^{114/110}$Cd values of both solutions and solids increase when increasing the fraction of Cd^{2+} adsorbed to Mn dioxides, and those of the solutions are greater than those of the solids (Figure 1c,d). This indicates that lighter Cd isotopes are preferentially enriched on mineral surfaces, with heavier isotopes remaining in the solution. As proportions of Cd adsorbed increase from 28.2 to 95.6% for TBir and from 59.4 to 90.0% for HBir over the 4−8 pH range, Cd isotope fractionations ($\Delta^{114/110}\mathrm{Cd}_{\text{solid-solution}}$) are almost the same for the two systems: −1.47 ± 0.09‰ (1SD; $n = 5$) for TBir and −0.88 ± 0.03‰ (1SD; $n = 5$) for HBir (Tables S4 and S5).

Both equilibrium and Rayleigh models were considered to fit the Cd isotope fractionation processes induced by adsorption. These models are described by eqs 3 and 4:

$$\delta^{114/110}\mathrm{Cd}_{\mathrm{solution}} = \frac{\delta^{114/110}\mathrm{Cd}_{\mathrm{stock}} - 1000 \cdot f \cdot (\alpha_{\mathrm{solid-solution}} - 1)}{1 - f \cdot (f \cdot \alpha_{\mathrm{solid-solution}})} \quad \text{(equilibrium model)} \tag{3}$$

$$\delta^{114/110}\mathrm{Cd}_{\mathrm{solution}} = (1000 + \delta^{114/110}\mathrm{Cd}_{\mathrm{stock}}) \cdot (1 - f)^{(\alpha_{\mathrm{solid-solution}} - 1)} - 1000 \quad \text{(Rayleigh model)} \tag{4}$$

where $\alpha_{\text{solid-solution}}$ refers to the estimated isotope fractionation factor between adsorbed and aqueous Cd, f is the proportion of Cd adsorbed, and $\delta^{114/110}\mathrm{Cd}_{\text{stock}}$ is the isotopic composition of the stock solution.

Consistent with previous studies, Cd isotopic fractionation on Mn dioxides is best described by the equilibrium model.[7,40] The fractionation factors ($\alpha_{\text{adsorbed-aqueous}}$) are 0.99846 ± 0.00011 for TBir and 0.99904 ± 0.00006 for HBir. The theoretical isotopic fractionation between adsorbed and aqueous Cd can be calculated according to eq 5.

$$\Delta^{114/110}\mathrm{Cd}_{\mathrm{solid-solution}} \cong 1000 \times \ln \alpha_{\mathrm{solid-solution}} \tag{5}$$

As-derived $\Delta^{114/110}\mathrm{Cd}_{\text{solid-solution}}$ values are −1.54 ± 0.11 and −0.96 ± 0.06‰ for TBir and HBir, respectively, consistent with measured values. These results suggest that the magnitude and direction of Cd isotope fractionation during the adsorption of Mn dioxides may be controlled by differences in the bonding environments between aqueous and adsorbed Cd, independent of the reaction conditions (e.g., reaction time and pH).

3.2. Cd Binding Environments Revealed by Cd K-edge EXAFS Analysis.

The Cd K-edge EXAFS spectra of typical Cd-adsorbed Mn dioxides were collected to reveal the Cd coordination mechanisms at the mineral surfaces. The k^2-weighted EXAFS spectra and corresponding Fourier transforms (FTs) of the Cd^{2+}-adsorbed samples are distinct from those of the $\mathrm{Cd(NO_3)_2}$ solution and $\mathrm{Cd(OH)_2}$ (Figure 2), indicating the formation of inner-sphere complexes at mineral surfaces and the absence of $\mathrm{Cd(OH)_2}$ precipitates. In the FTs of Cd^{2+}-adsorbed samples, the peak at $R + \Delta R \sim 1.8$ Å corresponds to the first shell of Cd−O pairs, while the peak at $R + \Delta R \sim 3.2$ Å may be assigned to Mn backscattering.[33,36]

Cd K-edge EXAFS spectra were then analyzed by shell-by-shell fitting, taking into consideration whether a third cumulant was in the first Cd−O shell. The addition of such a third cumulant greatly improves fit quality for Cd adsorbed samples, e.g., reducing R-factor, χ^2, and reduced χ^2 by 16−19, 16−19, and 1−3%, respectively, compared to that without a third cumulant (Tables 1 and S6). In addition, average Cd−O distances within this first Cd−O shell are slightly longer (2.28 ± 0.03 and 2.28 ± 0.04 Å for HBir and TBir, respectively) when using this third cumulant than those derived without it (2.24 ± 0.01 and 2.23 ± 0.01 Å), while they are similar for $\mathrm{Cd(NO_3)_2}$ (2.27 ± 0.02 vs 2.27 ± 0.01 Å). All these results indicate the formation of highly distorted Cd octahedra when adsorbed onto the birnessite surfaces.[7,57]

The Cd−Mn shell was fitted with a single Cd−Mn path, resulting in similar Cd−Mn distances of 3.66−3.67 Å but different coordination numbers (CNs), 10.9 ± 3.3 and 2.8 ± 0.9 for HBir and TBir, respectively. The much higher CN derived for Cd sorbed on HBir suggests that it is predominantly forming TCS complexes at HBir vacant sites.[33,36] Furthermore, the large Debye−Waller factor (σ^2 = 0.0150) of this Cd−Mn shell (Table 1) may indicate the formation of a minor amount of DCS complexes at HBir layer edge sites.[33,36] For TBir, CN and R of the Cd−Mn pairs are consistent with the formation of DCS complexes at layer edge sites.[36]

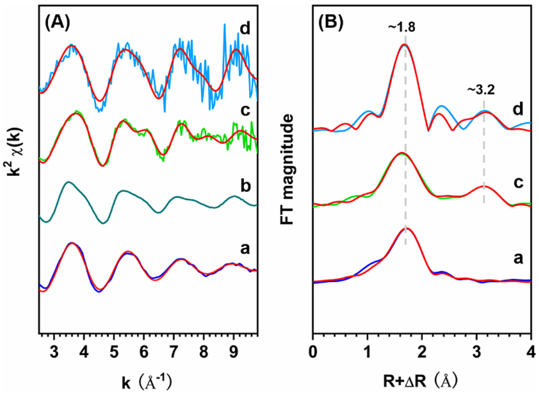

Figure 2. k^2-weighted Cd K-edge EXAFS spectra (A) of aqueous $\mathrm{Cd(NO_3)_2}$ (a) and $\mathrm{Cd(OH)_2}$ (b) standards, Cd-adsorbed HBir (c), and TBir (d) samples, and the corresponding Fourier transforms (FTs, B), overlaid with the best fits with the addition of a third cumulant in the first Cd−O shell fitting for HBir and TBir. The experimental data and the best fits are shown as colored and red lines, respectively. The initial Cd concentrations were 133.4 μM for TBir and 177.9 μM for HBir in the pH-edge experiments, and the initial concentrations of the mineral suspensions were 0.5 g·L^{-1} for TBir and 0.1 g·L^{-1} for HBir, with a background electrolyte of 0.1 M $\mathrm{NaNO_3}$ solution, pH 7.

3.3. Geometry Optimization of Cd Surface Species on Birnessites.

From the simulations of reference CdO, $\mathrm{Cd(OH)_2}$, and $\mathrm{Cd(NO_3)_2}$ structures, DFT calculations appear to overestimate the dimensions of experimental structures by less than 3% (Table 2). CdO and $\mathrm{Cd(OH)_2}$ have symmetrical octahedral Cd coordination. Their optimized lattice parameters are a = 4.796 Å and c = 2.398 Å for CdO and a = 3.593 Å and c = 4.829 Å for $\mathrm{Cd(OH)_2}$, whereas experimentally determined parameters are a = 4.770 Å and c = 2.353 Å for CdO[68] and a = 3.194 Å and c = 4.702 Å for $\mathrm{Cd(OH)_2}$.[69] In $\mathrm{Cd(NO_3)_2}$, the 6-fold coordination of Cd is asymmetric. The DFT-calculated lattice parameters of $\mathrm{Cd(NO_3)_2}$ are a = 7.877, c = 7.853, and b = 15.992 Å, which are 4.0−4.9% greater than experimental values (a = c = 7.507 Å, b = 15.369 Å).[70] The average d(Cd−O) in $\mathrm{Cd(NO_3)_2}$, CdO, and $\mathrm{Cd(OH)_2}$ are larger than the experimental values (2.33 Å,[70] 2.35 Å,[68] and 2.31 Å[69]) by less than 3%.

Table 2 lists the results of DFT geometry optimization for Cd surface complexes formed at birnessite surfaces. The wide variation of d(Cd−O) for Cd complexes indicates highly distorted octahedral coordination and d<Cd−O> of the TCS complex is smaller than that of edge species such as DCS, DESI, and DESII complexes (Figure S5), the d<Cd−O> of the TES complex being similar to those of the edge species. On the other hand, TCS shows larger d<Cd−Mn>, than edge species. In contrast with d <Cd−O>, d <Cd−Mn> significantly differs among edge species. This makes this parameter more suitable than d<Cd−O> for species identification based on structural parameters. However, it should be noted that the present calculations of d<Cd−Mn> for edge species were based on Cd^{2+} binding to Mn(IV) sites, and are expected to be shorter

Table 1. Fitting Results of the EXAFS Spectra for Aqueous $Cd(NO_3)_2$ Standard and Typical Cd-adsorbed Samples, Including a Third Cumulant (Cum.) in the First Cd−O Coordination Shell Fitting

sample	path	CN	R (Å)	σ^2 (Å^2)	third cum.	ΔE (eV)	reduced χ^2	χ^2	R-factor
$Cd(NO_3)_{2,\ aq}$	Cd−O	7.8 ± 0.5	2.27 ± 0.02 (2.27 ± 0.01)	0.0101 ± 0.0010	0.0001 ± 0.0004	2.9 ± 1.2	545.91	4768.76	0.0063
HBir	Cd−O	8.2 ± 0.8	2.28 ± 0.03 (2.24 ± 0.01)	0.0113 ± 0.0016	0.0009 ± 0.0008	3.4 ± 2.0	3.72	15.71	0.0054
	Cd−Mn	10.9 ± 3.3	3.66 ± 0.05	0.0150 ± 0.0035					
TBir	Cd−O	5.9 ± 1.0	2.28 ± 0.04 (2.23 ± 0.01)	0.0001 ± 0.0018	0.0008 ± 0.0008	2.2 ± 3.2	1.60	10.79	0.0372
	Cd−Mn	2.8 ± 0.9	3.67 ± 0.03	0.0030[a]					

[a] Fixed during fitting.

Table 2. DFT-calculated Interatomic Distances (in Å) of Cd in Solid Phases

				surface complexes on birnessite				
	CdO	$Cd(OH)_2$	$Cd(NO_3)_2$	TES	TCS	DCS	DESI	DESII
d(Cd−O)	2.40	2.35	2.37	2.40	2.30	2.22	2.23	2.31
	2.40	2.35	2.37	2.38	2.31	2.24	2.30	2.49
	2.40	2.35	2.37	2.46	2.29	2.36	2.42	2.32
	2.40	2.35	2.39	2.30	2.36	2.42	2.44	2.30
	2.40	2.35	2.39	2.33	2.36	2.49	2.33	2.42
	2.40	2.35	2.44	2.30	2.36	2.50	2.42	2.32
	<2.40>	<2.35>	<2.39>	<2.36>	<2.33>	<2.37>	<2.36>	<2.36>
d(Cd−Mn)				3.18	3.70	3.54	3.17	3.18
				3.35	3.72	3.57	3.22	3.36
				3.36	3.70			4.19
					3.70			
					3.70			
					3.70			
				<3.29>	<3.70>	<3.56>	<3.19>	<3.57>

than that for Cd^{2+} binding to Mn(III) sites.[36] This limitation of DFT calculations may also account for the similar d<Cd−Mn> computed for TCS Cd^{2+} on HBir and DCS Cd^{2+} on TBir (Table 1).

3.4. Cd Isotope Fractionations onto Birnessite Edge Sites and Vacancies.

Since Cd^{2+} may be adsorbed onto hexagonal birnessite edge and vacant layer sites, relative proportions of Cd binding at these sites were first quantified from SCM modeling. The modeling of Cd^{2+} adsorption data over the pH range of 4−8 fits satisfactorily the data (Figure 3 and Table S7) and shows that vacancy sites are the dominant active sites for Cd^{2+} adsorption onto HBir. With increasing pH conditions, the contribution of vacancies slightly decreases, however, to the benefit of edge sites. In detail, at pH 4, 59% of the total Cd adsorbed onto the solids is adsorbed onto vacancies, while at pH 8, 39% of the total Cd retained on the solid is located on the edge sites, with the rest being adsorbed at vacancies. Over the whole pH range, no $Cd(OH)_2$ is formed.

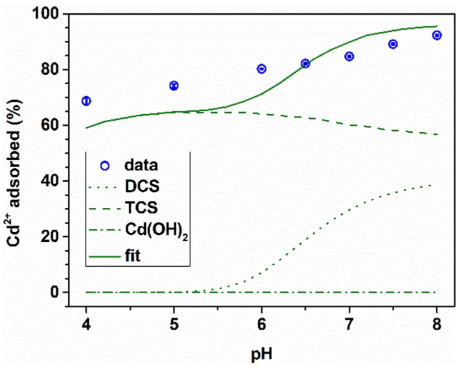

Figure 3. Modeling of Cd^{2+} adsorption edges on HBir over the pH range of 4−8. The experimental conditions were as follows: initial Cd^{2+} concentration = 177.9 μM, reaction time = 72 h, ionic strength = 0.1 M $NaNO_3$ solution, solid/solution ratio = 0.1 g·L^{-1}, and temperature = 25 ± 2 °C.

Because triclinic birnessite is commonly recognized as vacancy-free[18,71,72] and only adsorbs heavy metals onto edge sites, the theoretical $\Delta^{114/110}Cd_{\text{solid-solution}}$ of −1.54 ± 0.11‰ induced by Cd adsorption to TBir should thus be that of edge sites. This value was also used for fractionation induced during Cd adsorption to HBir edge sites. If the proportions of Cd adsorbed to HBir edge sites and vacancies are f_1 and f_2, respectively, and $\Delta^{114/110}Cd_{\text{edge-solution}}$ and $\Delta^{114/110}Cd_{\text{vacancy-solution}}$ the isotopic fractionation induced by adsorption at these sites, the overall $\Delta^{114/110}Cd_{\text{solid-solution}}$ induced by Cd adsorption can be expressed according to eq 6:

$$\Delta^{114/110}Cd_{\text{solid}-\text{solution}} = \frac{f_1}{f_1 + f_2} \times \Delta^{114/110}Cd_{\text{edge}-\text{solution}} + \frac{f_2}{f_1 + f_2} \times \Delta^{114/110}Cd_{\text{vacancy}-\text{solution}} \quad (6)$$

As a result, calculated values of $\Delta^{114/110}Cd_{\text{vacancy-solution}}$ at pH 4, 5, 6, 7, and 8 are −0.92 ± 0.11, −0.83 ± 0.11, −0.80 ± 0.12, −0.55 ± 0.18, and −0.43 ± 0.22‰, respectively, leading to an average $\Delta^{114/110}Cd_{\text{vacancy-solution}}$ of −0.71 ± 0.21‰.

Alternatively, it is possible to hypothesize that, at a given pH, the Cd^{2+} adsorption density on edge sites is similar for HBir and TBir. In this case, the proportions of Cd^{2+} on HBir edge sites are calculated to be 6, 7, 9, 13, and 16% of the total Cd^{2+} adsorbed at pH 4, 5, 6, 7, and 8, respectively. The $\Delta^{114/110}Cd_{\text{vacancy-solution}}$ values may then be calculated and range from −0.75 ± 0.14 to −0.89 ± 0.12‰, with an average of −0.80 ± 0.05‰. Both sets of values match those derived from the SCM modeling.

3.5. Cd Isotope Fractionation Mechanism. Our results show that lighter Cd isotopes are preferentially adsorbed on birnessite surfaces, consistent with previous studies.[40] As a general rule, heavy isotopes are preferred in stronger binding environments (e.g., shorter bond lengths). The enrichment of light Cd isotopes on iron (oxyhydr)oxides is attributed to the adsorption of highly distorted CdO_6 octahedra on mineral surfaces.[7] In the present study, both Cd K-edge EXAFS results and DFT geometry optimization analyses indicate that Cd mainly exists as a distorted octahedral complex when adsorbed to birnessite surfaces. This probably accounts for the enrichment of light Cd isotopes onto solids. In addition, the exchange of various aqueous Cd species may also affect the isotope fractionation. Theoretical calculations of aqueous Cd species under current experimental conditions (pH range of 4−8) show that Cd mainly exists as Cd^{2+} (84−87%) and $Cd(NO_3)^+$ (∼12%) with negligible amounts of $Cd(NO_3)_2$, $Cd(OH)^+$, $Cd(HCO_3)^+$, and $CdCO_{3,aq}$ (Figure S9). Compared to $Cd(NO_3)^+$, Cd^{2+} preferentially sorbs to birnessite surfaces, owing to its larger positive charge, thus contributing to the enrichment of light Cd isotopes onto solids, as $Cd(NO_3)^+$ is isotopically slightly heavier than Cd^{2+}.[73]

Values of $\Delta^{114/110}Cd_{solid\text{-}solution}$ derived from the equilibrium model are −1.54 ± 0.11 and −0.96 ± 0.06‰ for TBir and HBir, respectively. Analysis of isotopic fractionation kinetic (Figure S7) and modeling of the solution and solid isotopic compositions all show that equilibrium fractionation, rather than kinetic effects, causes the isotope offsets observed in the present system. In addition, the magnitude of Cd isotope fractionation induced by adsorption to TBir is greater compared to HBir, most likely owing to the different binding sites and complex structures of Cd adsorbed on the minerals. For comparison, Cd isotope fractionation resulting from its adsorption to different Fe (hydr)oxides is similar, with consistent $\Delta^{114/110}Cd_{solid\text{-}solution}$ values of −0.5‰ for goethite, hematite, and ferrihydrite.[7] A similar effect was reported for the sorption of other heavy metals to birnessite-like minerals. For example, light Zn isotopes are enriched at hexagonal birnessite vacant sites, while heavy isotopes are bound at edge sites.[33] Considering the local environments of Cd^{2+} sorbed to birnessite vacancies and edge sites (Figure 3, Tables 1 and 2), it is reasonable to expect different isotope fractionation magnitudes onto the two types of active sites. Consistently, Cd isotope fractionations induced by adsorption to edge sites ($\Delta^{114/110}Cd_{edge\text{-}solution}$) and vacancies ($\Delta^{114/110}Cd_{vacancy\text{-}solution}$) are −1.54 ± 0.11 and −0.71 ± 0.21‰, respectively. Several factors may account for this difference. First, although Cd K-edge EXAFS analysis indicates similar Cd−O distances in both cases (Table 1), DFT geometry optimization supports a shorter average Cd−O distance (2.33 Å) for TCS complexes on birnessite vacancies than that for DCS and DES complexes on edge sites (2.36−2.37 Å) (Table 2). Second, CNs for Cd−Mn shells may also influence isotope fractionation, and EXAFS analysis indicates TCS complexes with large Cd−Mn CNs for Cd^{2+} sorbed at vacancies and DCS complexes with low Cd−Mn CNs at birnessite edge sites (Table 1). Previous studies suggested indeed that the greater magnitudes of Sb and Ni isotope fractionation on goethite compared to ferrihydrite were probably due to the formation of weaker surface complexes with lower CNs for Sb/Ni−Fe pairs on goethite.[74,75]

However, it should be noted that under acidic conditions Mn(III) initially present in TBir layers can disproportionate and migrate out of the layer, creating layer vacancies and leading to the transformation of triclinic birnessite to hexagonal birnessite.[21,22] This transformation is confirmed by the powder XRD analysis of the reaction product of TBir acidification at pH4 for 72 h (TBir_pH4_72h; Text S3 and Figure S10). If Mn^{3+} was released into the solution, a large portion of Cd^{2+} would adsorb at vacancy sites, increasing the Cd^{2+} adsorption density and decreasing the Cd isotope fractionation magnitude. This is not observed however as Cd^{2+} adsorption density on TBir remains much lower than that on HBir even under acidic conditions (e.g., 4−5, Table S3), and $\Delta^{114/110}Cd_{solid\text{-}solution}$ values induced by Cd^{2+} adsorption to TBir remain constant over the whole pH4−8 range (Table S4). This may be due to the presence of $Mn^{2+/3+}$ (coming from TBir layers) on at least one side of layer vacancies formed during TBir equilibration at low pH (e.g., TBir_pH4_72h), protons being present on the other side to compensate for the remaining layer charge deficit.[21] Analysis of the dissolved Mn concentration after equilibration of TBir at pH4 for 72 h indicates a negligible Mn release (4.00 ± 0.05% of total Mn), confirming the capping of newly formed layer vacancies by $Mn^{2+/3+}$. Exchanging Cd^{2+} for these cations may not be favored especially because of the ionic background electrolyte (0.1 M $NaNO_3$).[76] As a consequence, adsorption of Cd^{2+} occurs mainly onto layer edge sites over the whole pH range investigated, leading to similar Cd isotope fractionations on TBir.

Finally, the $\Delta^{114/110}Cd_{solid\text{-}solution}$ during Cd^{2+} adsorption onto HBir at pH 8 ± 0.05 (−0.87 ± 0.12‰) is larger than that previously reported (−0.24 to −0.56‰) for an analogous mineral.[40] This difference can be related to the relative proportions of Cd^{2+} on vacancies vs edge sites as our results show that the formation of DCS complexes at edge sites causes a larger isotope offset ($\Delta^{114/110}Cd_{edge\text{-}solution}$ = −1.54 ± 0.11‰) than that of TCS complexes on vacancies ($\Delta^{114/110}Cd_{vacancy\text{-}solution}$ = −0.71 ± 0.21‰); the more Cd adsorbed on edge sites, the greater the magnitude of isotope fractionation on the solid. Wasylenki et al. (2014) also revealed that isotope offsets decreased from −0.8‰ after 1 h reaction time to −0.2‰ after 912 h, as the result of Cd migration adsorbed to vacancy sites into the mineral structure,[40] which is unlikely owing to the ionic radius of Cd^{2+}. Alternatively, this kinetic effect may be caused by a modification in Cd binding mode from DCS and DES inner-sphere complexes on edges to TCS complexes on vacancies, owing to the decrease in the number of edge sites accompanying the aging and aggregation of birnessite nanoparticles under alkaline conditions (pH ∼ 8.3).[77]

4. ENVIRONMENTAL IMPLICATIONS

Cd isotopes have great potential for effectively tracking Cd sources and fate and understanding Cd behaviors. Due to their high scavenging ability, phyllomanganates are significant Cd reservoirs and thus mediate Cd geochemical cycling as well as its isotopic composition in natural environments. The present study shows that different Cd isotope fractionations stem from adsorption onto birnessite edge sites ($\Delta^{114/110}Cd_{edge\text{-}solution}$ = −1.54 ± 0.11‰) and vacancy sites ($\Delta^{114/110}Cd_{vacancy\text{-}solution}$ = −0.71 ± 0.21‰), thus providing a direct clue to the interpretation of isotopic signatures measured in natural settings. For example, the isotope fractionation

($\Delta^{114/110}Cd_{sediment-river}$) of −0.91 to −1.0‰ observed between water and sediments in acid mine drainage[4] can be accounted for by Cd adsorption to secondary oxides and hydroxides, and more especially to Mn (hydr)oxides. Similarly, magnitudes of Cd isotope fractionation on the birnessite edge and vacancy sites can be used as end members to assess isotopic offsets during Cd adsorption onto birnessite-like minerals, from relative proportions of Cd^{2+} at these sites. From a practical point of view, reconstruction of the isotope fractionation of solids by using the two end members may be used to assess the relative proportions of Cd^{2+} adsorbed onto birnessite edge sites and vacancies, which is currently challenging. The present results also suggest that these birnessite-like minerals may affect Cd isotope fractionation to a larger extent than other active components, such as Fe/Al (hydr)oxides, clay minerals, calcite, quartz, or humic acids.[42−44,78] In addition to birnessite structural characteristics, such as the relative proportions of vacancy and edge sites, different binding modes of Cd^{2+} adsorption onto Mn (hydr)oxides (e.g., tectomanganates with different tunnel sizes), and under contrasting environmental conditions (e.g., presence and nature of inorganic and organic ligands, temperature), may influence Cd isotope fractionation further.[7,40,44,78] Additional studies are thus needed to fully elucidate the intrinsic mechanisms and influencing factors of the directions and magnitudes of Cd isotopic fractionation during its interaction with environmentally relevant Mn (hydr)oxides.

■ ASSOCIATED CONTENT

Supporting Information

The Supporting Information is available free of charge at https://pubs.acs.org/doi/10.1021/acs.est.4c03808.

> Reagent information; powder XRD, SEM, and PZC of birnessite samples; structure determination of HBir using a specific trial-and-error method; DFT-calculated Cd surface complexes formed at different adsorption sites of birnessite; Cd^{2+} adsorption kinetics and pH edge experiments on TBir and HBir; Cd isotope fractionation kinetics during adsorption onto TBir; initial Cd concentrations, Cd adsorption density and fraction on birnessite samples in adsorption kinetics, pH edge experiments, and corresponding isotopic compositions of the solution and solid; fitting results of Cd K-edge EXAFS spectra for aqueous $Cd(NO_3)_2$ standard and typical Cd adsorbed samples, without a third cumulant for the first Cd−O shell fitting; experimental and modeling proportions of Cd adsorbed onto HBir edge sites and vacancies over a pH range of 4−8; changes in aqueous Cd species as a function of pH; and mineral transformation of TBir after acidification at pH4 (PDF)

■ AUTHOR INFORMATION

Corresponding Authors

Hui Yin − *Hubei Key Laboratory of Soil Environment and Pollution Remediation, College of Resources and Environment, Huazhong Agricultural University, Wuhan 430070, China*; orcid.org/0000-0003-3060-7025; Phone: +86 27 87280271; Email: yinhui666@mail.hzau.edu.cn; Fax: +86 27 87288618

Chuanwei Zhu − *School of Earth Sciences and Resources, Chang'An University, Xi'an 710054, China*; Email: zhuchuanwei@chd.edu.cn

Authors

Xinran Yan − *Hubei Key Laboratory of Soil Environment and Pollution Remediation, College of Resources and Environment, Huazhong Agricultural University, Wuhan 430070, China*

Kideok D. Kwon − *Department of Geology, Kangwon National University, Chuncheon 24347, Republic of Korea*

Xueyuan Gu − *State Key Laboratory of Pollution Control and Resource Reuse, School of the Environment, Nanjing University, Nanjing 210023, China*; orcid.org/0000-0002-8521-3667

Wei Zhao − *State Key Laboratory of Soil Erosion and Dryland Farming on the Loess Plateau, Northwest A&F University, Yangling, Shaanxi Province 712100, China*; orcid.org/0000-0002-6035-1836

Bruno Lanson − *Univ. Grenoble Alpes, Univ. Savoie Mont Blanc, CNRS, IRD, Univ. Gustave Eiffel, ISTerre, F-38000 Grenoble, France*; orcid.org/0000-0003-1187-3221

Wei Li − *Key Laboratory of Surficial Geochemistry, Ministry of Education, School of Earth Sciences and Engineering, Nanjing University, Nanjing 210023, China*; orcid.org/0000-0002-0789-0320

Jingyuan Ma − *Shanghai Synchrotron Radiation Facility, Shanghai Institute of Applied Physics, Chinese Academy of Sciences, Shanghai 201204, China*

Yan Li − *Beijing Key Laboratory of Mineral Environmental Function, School of Earth and Space Sciences, Peking University, Beijing 100871, China*

Jiangshan Li − *State Key Laboratory of Geomechanics and Geotechnical Engineering, Institute of Rock and Soil Mechanics, Chinese Academy of Sciences, Wuhan 430071, China*

Guohong Qiu − *Hubei Key Laboratory of Soil Environment and Pollution Remediation, College of Resources and Environment, Huazhong Agricultural University, Wuhan 430070, China*; orcid.org/0000-0002-1181-3707

Xionghan Feng − *Hubei Key Laboratory of Soil Environment and Pollution Remediation, College of Resources and Environment, Huazhong Agricultural University, Wuhan 430070, China*; orcid.org/0000-0001-5499-7174

Wenfeng Tan − *Hubei Key Laboratory of Soil Environment and Pollution Remediation, College of Resources and Environment, Huazhong Agricultural University, Wuhan 430070, China*

Hanjie Wen − *School of Earth Sciences and Resources, Chang'An University, Xi'an 710054, China*

Qiaoyun Huang − *Hubei Key Laboratory of Soil Environment and Pollution Remediation, College of Resources and Environment, Huazhong Agricultural University, Wuhan 430070, China*; orcid.org/0000-0002-2733-8066

Fan Liu − *Hubei Key Laboratory of Soil Environment and Pollution Remediation, College of Resources and Environment, Huazhong Agricultural University, Wuhan 430070, China*; orcid.org/0000-0003-0341-923X

Complete contact information is available at: https://pubs.acs.org/10.1021/acs.est.4c03808

Author Contributions

[&]H.Y. and K.D.K. contributed equally.

Notes

The authors declare no competing financial interest.

■ ACKNOWLEDGMENTS

The authors gratefully thank the National Natural Science Foundations of China (No. 42077015) and the Fundamental Research Funds for the Central Universities (Grant 103-510320036) for their financial support.

■ REFERENCES

(1) Godt, J.; Scheidig, F.; Grosse-Siestrup, C.; Esche, V.; Brandenburg, P.; Reich, A.; Groneberg, D. A.; Groneberg, D. A. The toxicity of cadmium and resulting hazards for human health. *J. Occup. Med. Toxicol.* **2006**, *1*, 22.

(2) Cullen, J. T.; Maldonado, M. T. Biogeochemistry of Cadmium and Its Release to the Environment. In *Cadmium: from toxicity to essentiality*; Springer, 2013.

(3) Imseng, M.; Wiggenhauser, M.; Müller, M.; Keller, A.; Frossard, E.; Wilcke, W.; Bigalke, M. The fate of Zn in agricultural soils: A stable isotope approach to anthropogenic impact, soil formation, and soil−plant cycling. *Environ. Sci. Technol.* **2019**, *53* (8), 4140−4149.

(4) Yang, W. J.; Ding, K. B.; Zhang, P.; Qiu, H.; Cloquet, C.; Wen, H. J.; Morel, J. L.; Qiu, R. L.; Tang, Y. T. Cadmium stable isotope variation in a mountain area impacted by acid mine drainage. *Sci. Total Environ.* **2019**, *646*, 696−703.

(5) Chrastný, V.; Čadková, E.; Vaněk, A.; Teper, L.; Cabala, J.; Komárek, M. Cadmium isotope fractionation within the soil profile complicates source identification in relation to Pb−Zn mining and smelting processes. *Chem. Geol.* **2015**, *405*, 1−9.

(6) Salmanzadeh, M.; Hartland, A.; Stirling, C. H.; Balks, M. R.; Schipper, L. A.; Joshi, C.; George, E. Isotope tracing of long-term cadmium fluxes in an agricultural soil. *Environ. Sci. Technol.* **2017**, *51* (13), 7369−7377.

(7) Yan, X.; Zhu, M.; Li, W.; Peacock, C. L.; Ma, J.; Wen, H.; Liu, F.; Zhou, Z.; Zhu, C.; Yin, H. Cadmium isotope fractionation during adsorption and substitution with iron (oxyhydr)oxides. *Environ. Sci. Technol.* **2021**, *55* (17), 11601−11611.

(8) Guinoiseau, D.; Galer, S. J. G.; Abouchami, W. Effect of cadmium sulphide precipitation on the partitioning of Cd isotopes: Implications for the oceanic Cd cycle. *Earth. Planet. Sci. Lett.* **2018**, *498*, 300−308.

(9) Wombacher, F.; Rehkämper, M.; Mezger, K.; Bischoff, A.; Münker, C. Cadmium stable isotope cosmochemistry. *Geochim. Cosmochim. Acta* **2008**, *72* (2), 646−667.

(10) Zhu, C.; Wen, H.; Zhang, Y.; Yin, R.; Cloquet, C. Cd isotope fractionation during sulfide mineral weathering in the Fule Zn-Pb-Cd deposit, Yunnan Province, Southwest China. *Sci. Total Environ.* **2018**, *616−617*, 64−72.

(11) Wiggenhauser, M.; Aucour, A. M.; Bureau, S.; Campillo, S.; Telouk, P.; Romani, M.; Ma, J. F.; Landrot, G.; Sarret, G. Cadmium transfer in contaminated soil-rice systems: Insights from solid-state speciation analysis and stable isotope fractionation. *Environ. Pollut.* **2021**, *269*, No. 115934.

(12) Feng, X. H.; Zhai, L. M.; Tan, W. F.; Zhao, W.; Liu, F.; He, J. Z. The controlling effect of pH on oxidation of Cr(III) by manganese oxide minerals. *J. Colloid Interface Sci.* **2006**, *298* (1), 258−266.

(13) Lefkowitz, J. P.; Elzinga, E. J. Structural alteration of hexagonal birnessite by aqueous Mn(II): Impacts on Ni(II) sorption. *Chem. Geol.* **2017**, *466*, 524−532.

(14) Vodyanitskii, Y. N. Mineralogy and geochemistry of manganese: A review of publications. *Eurasian Soil Science* **2009**, *42* (10), 1170−1178.

(15) Post, J. E. Manganese oxide minerals: Crystal structures and economic and environmental significance. *Proc. Natl. Acad. Sci. U.S.A.* **1999**, *96* (7), 3447−3454.

(16) Schmitt, A.-D.; Galer, S. J. G.; Abouchami, W. Mass-dependent cadmium isotopic variations in nature with emphasis on the marine environment. *Earth. Planet. Sci. Lett.* **2009**, *277* (1−2), 262−272.

(17) Horner, T. J.; Schönbächler, M.; Rehkämper, M.; Nielsen, S. G.; Williams, H.; Halliday, A. N.; Xue, Z.; Hein, J. R. Ferromanganese crusts as archives of deep water Cd isotope compositions. *Geochem. Geophys. Geosyst.* **2010**, *11* (4), 1−10.

(18) Drits, V. A.; Silvester, E.; Gorshkov, A. I.; Manceau, A. Structure of synthetic monoclinic Na-rich birnessite and hexagonal birnessite; I, Results from X-ray diffraction and selected-area electron diffraction. *Am. Mineral.* **1997**, *82* (9−10), 946−961.

(19) Silvester, E.; Manceau, A.; Drits, V. A. Structure of synthetic monoclinic Na-rich birnessite and hexagonal birnessite; II, Results from chemical studies and EXAFS spectroscopy. *Am. Mineral.* **1997**, *82* (9−10), 962−978.

(20) Drits, V. A.; Lanson, B.; Gorshkov, A. I.; Manceau, A. Substructure and superstructure of four-layer Ca-exchanged birnessite. *Am. Mineral.* **1998**, *83* (1−2), 97−118.

(21) Lanson, B.; Drits, V. A.; Silvester, E.; Manceau, A. Structure of H-exchanged hexagonal birnessite and its mechanism of formation from Na-rich monoclinic buserite at low pH. *Am. Mineral.* **2000**, *85* (5−6), 826−838.

(22) Manceau, A.; Drits, V. A.; Silvester, E.; Bartoli, C.; Lanson, B. Structural mechanism of Co2+ oxidation by the phyllomanganate buserite. *Am. Mineral.* **1997**, *82* (11−12), 1150−1175.

(23) Villalobos, M.; Escobar-Quiroz, I. N.; Salazar-Camacho, C. The influence of particle size and structure on the sorption and oxidation behavior of birnessite: I. Adsorption of As(V) and oxidation of As(III). *Geochim. Cosmochim. Acta* **2014**, *125*, 564−581.

(24) Villalobos, M.; Bargar, J.; Sposito, G. Mechanisms of Pb(II) sorption on a biogenic manganese oxide. *Environ. Sci. Technol.* **2005**, *39* (2), 569−576.

(25) Kwon, K. D.; Refson, K.; Sposito, G. Surface complexation of Pb(II) by hexagonal birnessite nanoparticles. *Geochim. Cosmochim. Acta* **2010**, *74* (23), 6731−6740.

(26) Lanson, B.; Drits, V. A.; Gaillot, A.; Silvester, E.; Plançon, A.; Manceau, A. Structure of heavy-metal sorbed birnessite: Part 1. Results from X-ray diffraction. *Am. Mineral.* **2002**, *87* (11−12), 1631−1645.

(27) Drits, V. A.; Lanson, B.; Bougerol-Chaillout, C.; Gorshkov, A. I.; Manceau, A. Structure of heavy-metal sorbed birnessite: Part 2. Results from electron diffraction. *Am. Mineral.* **2002**, *87* (11−12), 1646−1661.

(28) Manceau, A.; Lanson, B.; Drits, V. A. Structure of heavy metal sorbed birnessite. Part III: Results from powder and polarized extended X-ray absorption fine structure spectroscopy. *Geochim. Cosmochim. Acta* **2002**, *66* (15), 2639−2663.

(29) Yang, P.; Post, J. E.; Wang, Q.; Xu, W.; Geiss, R.; McCurdy, P. R.; Zhu, M. Metal adsorption controls stability of layered manganese oxides. *Environ. Sci. Technol.* **2019**, *53* (13), 7453−7462.

(30) Wang, Y.; Benkaddour, S.; Marafatto, F. F.; Pena, J. Diffusion- and pH-dependent reactivity of layer-type MnO_2: Reactions at particle edges versus vacancy sites. *Environ. Sci. Technol.* **2018**, *52* (6), 3476−3485.

(31) Peacock, C. L.; Sherman, D. M. Sorption of Ni by birnessite: Equilibrium controls on Ni in seawater. *Chem. Geol.* **2007**, *238* (1−2), 94−106.

(32) Manceau, A.; Steinmann, S. N. Density Functional theory modeling of the oxidation mechanism of Co(II) by birnessite. *ACS Earth Space Chem.* **2022**, *6* (8), 2063−2075.

(33) Wang, Z.; Peacock, C.; Kwon, K. D.; Gu, X.; Feng, X.; Li, W. Site-specific isotope fractionation during Zn adsorption onto birnessite: Insights from X-ray absorption spectroscopy, density functional theory and surface complexation modeling. *Geochim. Cosmochim. Acta* **2023**, *348*, 68−84.

(34) Grangeon, S.; Manceau, A.; Guilhermet, J.; Gaillot, A.-C.; Lanson, M.; Lanson, B. Zn sorption modifies dynamically the layer and interlayer structure of vernadite. *Geochim. Cosmochim. Acta* **2012**, *85*, 302−313.

(35) van Genuchten, C. M.; Peña, J. Sorption selectivity of birnessite particle edges: a d-PDF analysis of Cd(II) and Pb(II) sorption by δ-MnO_2 and ferrihydrite. *Environ. Sci.: Proc. Imp.* **2016**, *18* (8), 1030−1041.

(36) Sun, Q.; Cui, P. X.; Zhu, M.; Fan, T. T.; Ata-Ul-Karim, S. T.; Gu, J. H.; Wu, S.; Zhou, D. M.; Wang, Y. J. Cd(II) retention and remobilization on δ-MnO_2 and Mn(III)-rich δ-MnO_2 affected by Mn(II). *Environ. Int.* **2019**, *130*, No. 104932.

(37) Pokrovsky, O. S.; Viers, J.; Freydier, R. Zinc stable isotope fractionation during its adsorption on oxides and hydroxides. *J. Colloid Interface Sci.* **2005**, *291* (1), 192−200.

(38) Bryan, A. L.; Dong, S.; Wilkes, E. B.; Wasylenki, L. E. Zinc isotope fractionation during adsorption onto Mn oxyhydroxide at low and high ionic strength. *Geochim. Cosmochim. Acta* **2015**, *157*, 182−197.

(39) Sorensen, J. V.; Gueguen, B.; Stewart, B. D.; Peña, J.; Rouxel, O.; Toner, B. M. Large nickel isotope fractionation caused by surface complexation reactions with hexagonal birnessite. *Chem. Geol.* **2020**, *537*, No. 119481.

(40) Wasylenki, L. E.; Swihart, J. W.; Romaniello, S. J. Cadmium isotope fractionation during adsorption to Mn oxyhydroxide at low and high ionic strength. *Geochim. Cosmochim. Acta* **2014**, *140*, 212−226.

(41) Phillips, R. F.; Wang, Y.; Klein, F.; Farfan, G.; Ostrander, C. M.; Gadol, H.; Hansel, C. M.; Nielsen, S. G. The role of manganese oxide mineralogy in thallium isotopic fractionation upon sorption. *Geochim. Cosmochim. Acta* **2023**, *356*, 83−92.

(42) Komárek, M.; Ratié, G.; Vaňková, Z.; Šípková, A.; Chrastný, V. Metal isotope complexation with environmentally relevant surfaces: Opening the isotope fractionation black box. *Crit. Rev. Environ. Sci. Technol.* **2022**, *52* (20), 3573−3603.

(43) Wang, L.; Guo, J.; Tsang, D. C. W.; Hou, D. Cadmium isotope fractionation during sorption to soil minerals: Lab evidence and field implication. *Chem. Geol.* **2023**, *634*, No. 121607.

(44) Peng, H.; Liu, P.; Zheng, H.; Belshaw, N. S.; Hu, S.; Zhu, Z. Cadmium isotope fractionation during adsorption onto calcite. *Chem. Geol.* **2023**, *620*, No. 121341.

(45) Feng, X. H.; Liu, F.; Tan, W. F.; Liu, X. W. Synthesis of birnessite from the oxidation of Mn^{2+} by O_2 in alkali medium: Effects of synthesis conditions. *Clays Clay Miner.* **2004**, *52* (2), 240−250.

(46) McKenzie, R. M. The synthesis of birnessite, cryptomelane, and some other oxides and hydroxides of manganese. *Mineral. Mag.* **1971**, *38* (296), 493−502.

(47) Zhang, S.; Li, B.; Chen, Y.; Zhu, M.; Pedersen, J. A.; Gu, B.; Wang, Z.; Li, H.; Liu, J.; Zhou, X.-Q.; Hao, Y.-Y.; Jiang, H.; Liu, F.; Liu, Y.-R.; Yin, H. Methylmercury degradation by trivalent manganese. *Environ. Sci. Technol.* **2023**, *57* (14), 5988−5998.

(48) Lanson, B.; Marcus, M. A.; Fakra, S.; Panfili, F.; Geoffroy, N.; Manceau, A. Formation of Zn−Ca phyllomanganate nanoparticles in grass roots. *Geochim. Cosmochim. Acta* **2008**, *72* (10), 2478−2490.

(49) Patterson, A. L. The Scherrer formula for X-Ray particle size determination. *Phys. Rev.* **1939**, *56* (10), 978−982.

(50) Zhu, C.; Wen, H.; Zhang, Y.; Fan, H.; Fu, S.; Xu, J.; Qin, T. Characteristics of Cd isotopic compositions and their genetic significance in the lead-zinc deposits of SW China. *Sci. China Earth Sci.* **2013**, *56* (12), 2056−2065.

(51) Wen, H.; Zhang, Y.; Cloquet, C.; Zhu, C.; Fan, H.; Luo, C. Tracing sources of pollution in soils from the Jinding Pb−Zn mining district in China using cadmium and lead isotopes. *Appl. Geochem.* **2015**, *52*, 147−154.

(52) Zhang, Y.; Wen, H.; Zhu, C.; Fan, H.; Cloquet, C. Cadmium isotopic evidence for the evolution of marine primary productivity and the biological extinction event during the Permian-Triassic crisis from the Meishan section. *South China. Chem. Geol.* **2018**, *481*, 110−118.

(53) Ripperger, S.; Rehkämper, M. Precise determination of cadmium isotope fractionation in seawater by double spike MC-ICPMS. *Geochim. Cosmochim. Acta* **2007**, *71* (3), 631−642.

(54) Zhu, C.; Wu, Y.; Wen, H.; Wu, G.; Song, W.; Zhang, Y.; Zhao, B. High-precision double-spike Cd isotopic measurements of seawater by MC-ICP-MS and its application to seawater affected by hydrothermal vent fluids. *Acta Geochimica* **2023**, *42* (5), 934−942.

(55) Ravel, B.; Newville, M. ATHENA, ARTEMIS, HEPHAESTUS: data analysis for X-ray absorption spectroscopy using IFEFFIT. *J. Synchrotron Radiat.* **2005**, *12*, 537−541.

(56) Kelly, S. D.; Hesterberg, D.; Ravel, B. Analysis of Soils and Minerals Using X-ray Absorption Spectroscopy. In *Methods of Soil Analysis Part 5—Mineralogical Methods*; Soil Science Society of America: 2008; pp. 387−463.

(57) Bochatay, L.; Persson, P. Metal ion coordination at the water−Manganite (γ-MnOOH) interface: II An EXAFS study of zinc(II). *J. Colloid Interface Sci.* **2000**, *229*, 593−599.

(58) Li, Y.; Zhao, X.; Wu, J.; Gu, X. Surface complexation modeling of divalent metal cation adsorption on birnessite. *Chem. Geol.* **2020**, *551*, No. 119774.

(59) Keizer, M.; Van Riemsdijk, W. *ECOSAT: A computer program for the calculation of Speciation and Transport in soil-water systems, version 4.9 user's manual*; Wageningen University, 2009.

(60) Kinniburgh, D. *Fit User Guide Technical Report WD/93/23*; British Geological Survey: Keyworth, Nottinghamshire, 1993.

(61) Clark, S. J.; Segall, M. D.; Pickard, C. J.; Hasnip, P. J.; Probert, M. I. J.; Refson, K.; Payne, M. C. First principles methods using CASTEP. *Zeitschrift für Krist.* **2005**, *220* (5−6), 567−570.

(62) Perdew, J.; Burke, K.; Ernzerhof, M. Generalized gradient approximation made simple. *Phys. Rev. Lett.* **1996**, *77*, 3865−3868.

(63) Vanderbilt, D. Soft self-consistent pseudopotentials in a generalized eigenvalue formalism. *Phys. Rev. B* **1990**, *41* (11), 7892−7895.

(64) Monkhorst, H. J.; Pack, J. D. Special points for Brillouin-zone integrations. *Phys. Rev. B* **1976**, *13* (12), 5188−5192.

(65) Momma, K.; Izumi, F. VESTA 3 for three-dimensional visualization of crystal, volumetric and morphology data. *J. Appl. Crystallogr.* **2011**, *44* (6), 1272−1276.

(66) Della Puppa, L.; Komárek, M.; Bordas, F.; Bollinger, J.; Joussein, E. Adsorption of copper, cadmium, lead and zinc onto a synthetic manganese oxide. *J. Colloid Interface Sci.* **2013**, *399*, 99−106.

(67) Feng, X. H.; Zhai, L. M.; Tan, W. F.; Liu, F.; He, J. Z. Adsorption and redox reactions of heavy metals on synthesized Mn oxide minerals. *Environ. Pollut.* **2007**, *147* (2), 366−373.

(68) Liu, H.; Mao, H.; Somayazulu, M.; Ding, Y.; Meng, Y.; Häusermann, D. B1-to-B2 phase transition of transition-metal monoxide CdO under strong compression. *Phys. Rev. B* **2004**, *70* (9), No. 094114.

(69) Hemmingsen, L.; Bauer, R.; Bjerrum, M. J.; Schwarz, K.; Blaha, P.; Andersen, P. Structure, chemical bonding, and nuclear quadrupole interactions of β-$Cd(OH)_2$: Experiment and first principles calculations. *Inorg. Chem.* **1999**, *38* (12), 2860−2867.

(70) Louër, M.; Louër, D.; Grandjean, D. Structure cristalline et polymorphisme du nitrate de cadmium anhydre. *J. Solid State Chem.* **1976**, *17* (3), 231−237.

(71) Post, J. E.; Heaney, P. J.; Hanson, J. Rietveld refinement of a triclinic structure for synthetic Na-birnessite using synchrotron powder diffraction data. *Powder Diffr.* **2002**, *17* (3), 218−221.

(72) Lanson, B.; Drits, V. A.; Feng, Q.; Manceau, A. Structure of synthetic Na-birnessite: Evidence for a triclinic one-layer unit cell. *Am. Mineral.* **2002**, *87* (11−12), 1662−1671.

(73) Yang, J.; Li, Y.; Liu, S.; Tian, H.; Chen, C.; Liu, J.; Shi, Y. Theoretical calculations of Cd isotope fractionation in hydrothermal fluids. *Chem. Geol.* **2015**, *391*, 74−82.

(74) Zhou, W.; Zhou, J.; Feng, X.; Wen, B.; Zhou, A.; Liu, P.; Sun, G.; Zhou, Z.; Liu, X. Antimony isotope fractionation revealed from EXAFS during adsorption on Fe (oxyhydr)oxides. *Environ. Sci. Technol.* **2023**, *57* (25), 9353−9361.

(75) Gueguen, B.; Sorensen, J. V.; Lalonde, S. V.; Peña, J.; Toner, B. M.; Rouxel, O. Variable Ni isotope fractionation between Fe-oxyhydroxides and implications for the use of Ni isotopes as geochemical tracers. *Chem. Geol.* **2018**, *481*, 38−52.

(76) Tonkin, J. W.; Balistrieri, L. S.; Murray, J. W. Modeling sorption of divalent metal cations on hydrous manganese oxide using the diffuse double layer model. *Appl. Geochem.* **2004**, *19* (1), 29−53.

(77) Shi, M.; Li, Q.; Wang, Q.; Yan, X.; Li, B.; Feng, L.; Wu, C.; Qiu, R.; Zhang, H.; Yang, Z.; Yang, W.; Liao, Q.; Chai, L. A review on the transformation of birnessite in the environment: Implication for the stabilization of heavy metals. *J. Environ. Sci.* **2024**, *139*, 496−515.

(78) Ratié, G.; Chrastný, V.; Guinoiseau, D.; Marsac, R.; Vaňková, Z.; Komárek, M. Cadmium isotope fractionation during complexation with humic acid. *Environ. Sci. Technol.* **2021**, *55* (11), 7430−7444.

Cadmium Isotope Fractionation during Adsorption onto Edge Sites and Vacancies in Phyllomanganate

Hui Yin[1,#,*], Xinran Yan[1], Chuanwei Zhu[2,*], Kideok D. Kwon[3,#], Xueyuan Gu[4], Wei Zhao[5], Bruno Lanson[6],Wei Li[7], Jingyuan Ma[8], Yan Li[9], Jiangshan Li[10], Guohong Qiu[1], Xionghan Feng[1], Wenfeng Tan[1], Hanjie Wen[2], Qiaoyun Huang[1], Fan Liu[1]

[1]Hubei Key Laboratory of Soil Environment and Pollution Remediation, College of Resources and Environment, Huazhong Agricultural University, Wuhan 430070, China

[2]School of Earth Sciences and Resources, Chang'An University, Xi'an 710054, China

[3]Department of Geology, Kangwon National University, Chuncheon 24347, Republic of Korea

[4]State Key Laboratory of Pollution Control and Resource Reuse, School of the Environment, Nanjing University, 163, Xianlin Ave., Nanjing 210023, China

[5]State Key Laboratory of Soil Erosion and Dryland Farming on the Loess Plateau, Northwest A&F University, Yangling, Shaanxi Province 712100, China

[6]Univ. Grenoble Alpes, Univ. Savoie Mont Blanc, CNRS, IRD, Univ. Gustave Eiffel, ISTerre, F-38000 Grenoble, France

[7]Key Laboratory of Surficial Geochemistry, Ministry of Education, School of Earth Sciences and Engineering, Nanjing University, Nanjing 210023, China

[8]Shanghai Synchrotron Radiation Facility, Shanghai Institute of Applied Physics, Chinese Academy of Sciences, Shanghai 201204, China

[9]Beijing Key Laboratory of Mineral Environmental Function, School of Earth and Space Sciences, Peking University, Beijing 100871, China

[10]State Key Laboratory of Geomechanics and Geotechnical Engineering, Institute of Rock and Soil Mechanics, Chinese Academy of Sciences, Wuhan 430071, China

[#]These two authors contribute equally.

[*]Corresponding Authors: Tel.: +86 27 87280271. Fax: +86 27 87288618.

Email: yinhui666@mail.hzau.edu.cn; zhuchuanwei@chd.edu.cn.

Summary: 16 pages, 10 figures, 7 tables and 3 texts.

Text S1 Reagent information.

Cadmium(II) stock solution (1000 μg·mL^{-1}) was purchased from Guobiao Testing & Certification Co., Ltd, China, and $MnCl_2 \cdot 4H_2O$ (≥99%), $KMnO_4$ (≥99.5%), NaOH (≥96%), $NaNO_3$ (≥ 99%), HNO_3 (65-68%) and HCl (36-38%) were acquired from Sinopharm Chemical reagent Co., Ltd, China.

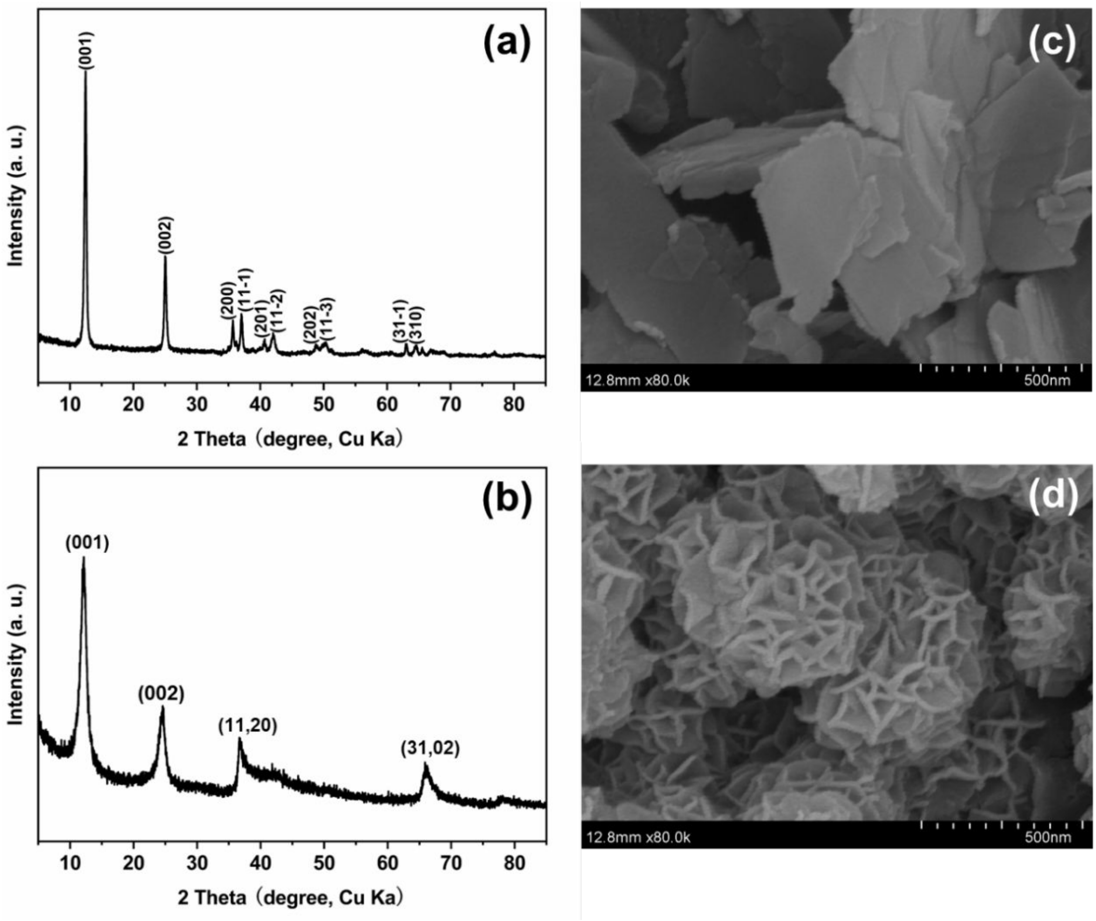

Figure S1 The XRD and SEM patterns of TBir (a and c) and HBir (b and d).

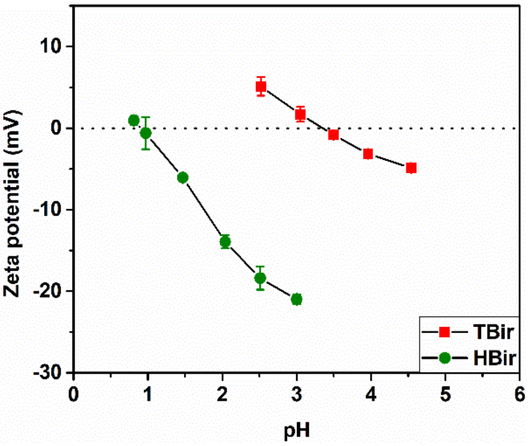

Figure S2 Zeta potentials of hexagonal (HBir) and triclinic birnessite (TBir) samples at pH values from 0-5 (the solid concentration is 0.1 g·L^{-1}).

Text S2 Structure determination of hexagonal turbostratic birnessite HBir.

In order to determine the microstructural characteristics of the hexagonal turbostratic birnessite sample HBir, high resolution powder XRD pattern was collected at a scan speed of 10 s per 0.04° 2θ on a Bruker D8 Advance diffractometer. Then the microstructural features of the sample was determined by a specific trial-and-error method[1-3]. During the fitting, some constraints were used. The average Mn oxidation state of HBir was determined to be 4.02±0.01 by the potentiometric titration method [2]. This means that HBir has neither layer Mn(III) nor interlayer Mn cations, and the only source of layer charge deficit is the presence of layer vacancies, which is solely compensated for by the presence of interlayer K. The K/Mn molar ratio was fixed the same to that of chemical composition analysis. The weight loss calculated from the thermogravimetric analysis (Figure S3) is 6.1% from 110-200 °C[4], and this leads to the presence of 0.33 H_2O molecules per octahedron. Thus the structural formula is thus $K_{0.22}(Mn_{0.94}\square_{0.06})O_2 \cdot 0.33H_2O$ (□ denotes vacancy). As usual an orthogonal setting was used for the unit cell with a =4.922 Å, b = 2.842 Å and c^* = 7.20 Å. The atomic positions of layer Mn and O and interlayer K were quite similar to those refined for KBi800 by Gaillot et al. 2003[4] or in KBi1000 by Gaillot et al. 2007[5] (Table S1). Two set of split positions for interlayer H_2O molecules were used. The first set were also quite similar to those reported in the aforementioned our two previous papers (Gaillot et al. 2003 and 2007) while the second set (bold) were refined independently here. Coherent scattering domain (CSD) size in the ab plane was calculated to be 180 Å by modelling the 20,11 diffraction band or 160 Å by modeling the 02,31 band. The final calculated powder XRD pattern matches the experimental data quite well (Figure S4).

Table S1 Atomic coordinates and site occupancies of HBir.

Atom	x	y	ζ (Å)	Occ.
Mn_{layer}	0.0000	0.000	0.00	0.940
O_{layer}	0.3330	0.000	1.00	1.000
O_{layer}	0.3330	0.000	-1.00	1.000
$K^{+}_{interlayer}$	-0.1670	0.000	3.60	0.036
$K^{+}_{interlayer}$	-0.4167	0.250	3.60	0.036
$K^{+}_{interlayer}$	-0.4167	-0.250	3.60	0.036
$K^{+}_{interlayer}$	0.1670	0.000	-3.60	0.036
$K^{+}_{interlayer}$	-0.4167	0.250	-3.60	0.036
$K^{+}_{interlayer}$	-0.4167	-0.250	-3.60	0.036
$H_2O_{interlayer}$	0.1000	0.000	3.60	0.025
$H_2O_{interlayer}$	-0.0500	0.150	3.60	0.025
$H_2O_{interlayer}$	-0.0500	-0.150	3.60	0.025
$H_2O_{interlayer}$	-0.1000	0.000	-3.60	0.025
$H_2O_{interlayer}$	0.0500	0.150	-3.60	0.025
$H_2O_{interlayer}$	0.0500	-0.150	-3.60	0.025
$H_2O_{interlayer}$	**-0.2530**	**0.000**	3.60	0.025
$H_2O_{interlayer}$	**-0.3730**	**0.120**	3.60	0.030
$H_2O_{interlayer}$	**-0.3730**	**-0.120**	3.60	0.030
$H_2O_{interlayer}$	**0.2530**	**0.000**	-3.60	0.030
$H_2O_{interlayer}$	**0.3730**	**0.120**	-3.60	0.030
$H_2O_{interlayer}$	**0.3730**	**-0.120**	-3.60	0.030

Note: Symmetry operations include (x, y, z), (-x, -y, -z), (x+½, y+½, z), and (-x + ½, -y+½, -z). Atomic coordinates x and y are expressed as fractions of the lattice parameters a (4.922 Å), and b (2.842 Å), respectively, while coordinate along the c^* axis, ζ, is expressed in Å. The lattice parameter c^* is fixed as 7.2 Å.

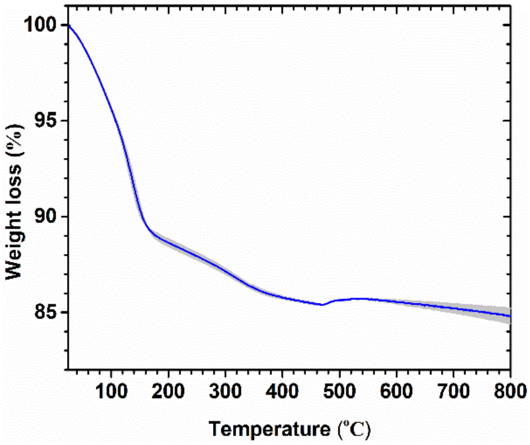

Figure S3 Thermogravimetric analysis of hexagonal birnessite HBir. The TGA curve is the average of 2 independent measurements, and the standard errors are shown as light gray shading. Data was collected on a NETZSCH TG 209 thermal analyser from ~25 to 800 °C with a heating rate of 10 °C·min^{-1} in dry air at a flow rate of 20 mL·min^{-1}.

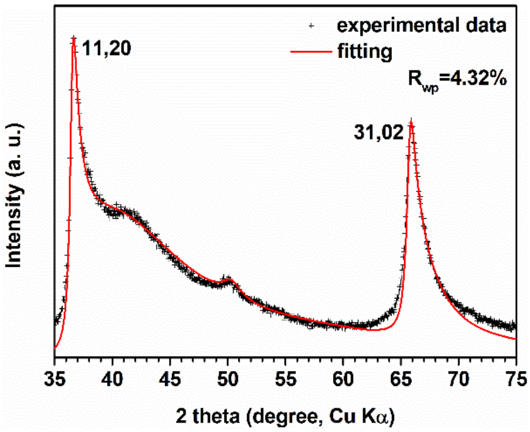

Figure S4 Comparison of the simulated powder XRD pattern (red solid line) with the experimental data (black crosses) of HBir over an interval of 35-75 ° 2 theta, Cu Kα.

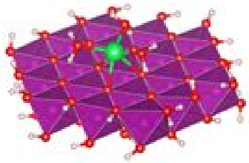

TES

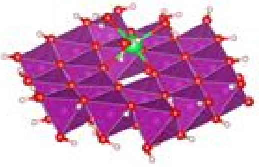

TCS

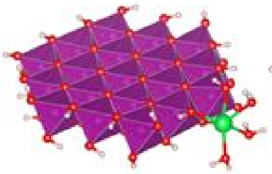

DESI

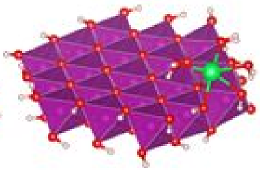

DESII

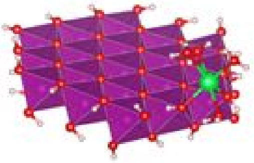

DCS

Figure S5 DFT-calculated cadmium (green) surface complexes formed at different adsorption sites of birnessite. TCS = triple-corner sharing, TES = triple-edge sharing, DES = double-edge sharing, DCS = double-corner sharing.

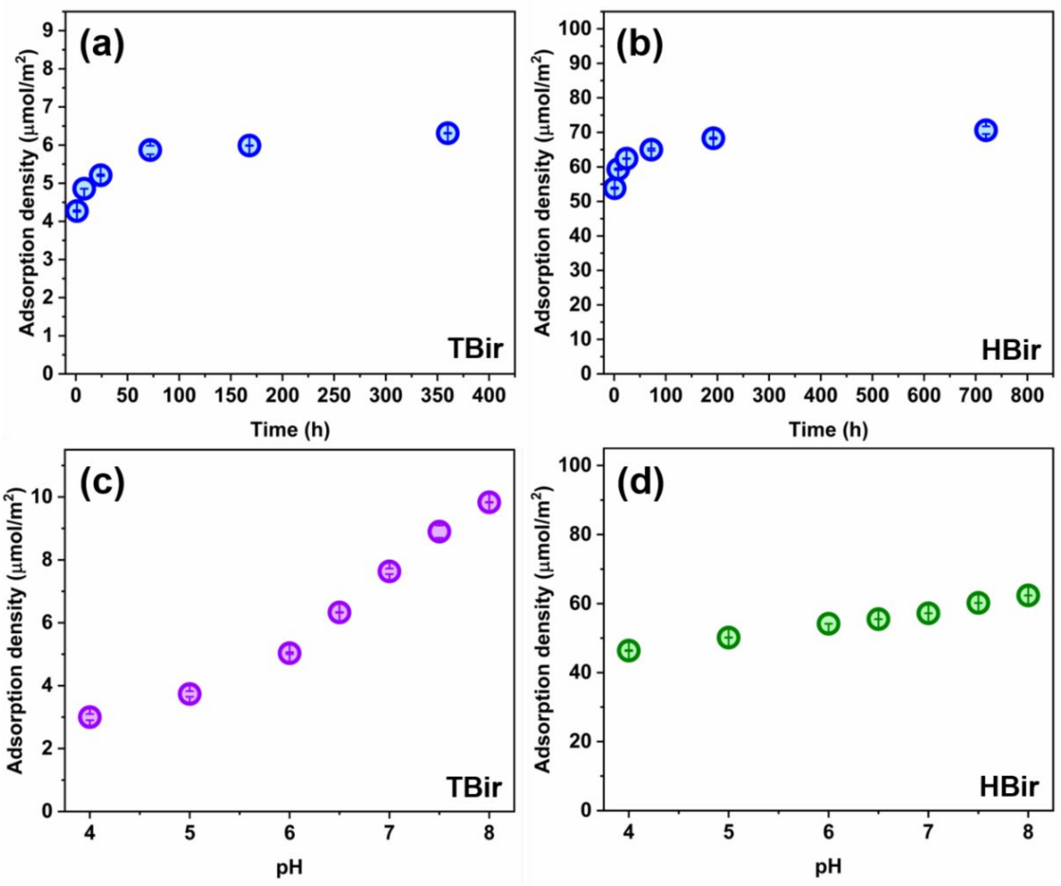

Figure S6 Adsorption kinetic experiments at pH 6 and pH edge experiments of Cd on TBir (a and c) and HBir (b and d) for 72 h. The Cd initial concentrations were set as 133.4 μM for TBir and 177.9 μM and 266.9 μM for HBir in pH edge and kinetic experiments, respectively. Mineral suspensions were 0.5 g·L^{-1} for TBir and 0.1 g·L^{-1} for HBir, with a background electrolyte of 0.1 M $NaNO_3$ solution.

Table S2 Initial Cd concentrations and Cd adsorption density and fraction of Cd adsorbed on HBir and TBir with time in adsorption kinetic experiments. Experimental conditions: pH = 6 ± 0.05, ionic strength = 0.1 M $NaNO_3$ solution, a solid/solution ratio of 0.5 $g \cdot L^{-1}$ for TBir and 0.1 $g \cdot L^{-1}$ for HBir, and temperature = 25 ± 2 ^{o}C.

Time (h)		Initial Cd (μM)		Cd adsorption density ($\mu mol \cdot m^{-2}$)		Fraction of Cd absorbed (%)	
TBir	HBir	TBir	HBir	TBir	HBir	TBir	HBir
1	1	133.4	266.9	4.27 ± 0.02	53.85 ± 0.22	41.5 ± 0.2	53.1 ± 0.2
8	8	133.4	266.9	4.86 ± 0.00	59.33 ± 0.24	47.2 ± 0.0	58.5 ± 0.2
24	24	133.4	266.9	5.21 ± 0.02	62.40 ± 0.09	50.6 ± 0.2	61.6 ± 0.1
72	72	133.4	266.9	5.87 ± 0.11	65.02 ± 0.32	57.0 ± 1.1	64.2 ± 0.3
168	192	133.4	266.9	5.99 ± 0.01	68.29 ± 0.21	58.2 ± 0.1	67.4 ± 0.2
360	720	133.4	266.9	6.31 ± 0.01	70.63 ± 1.21	61.3 ± 0.1	69.7 ± 1.1

Table S3 Initial Cd concentration, reaction pH and corresponding adsorption density and fraction of Cd adsorbed in pH edge experiments. Experimental conditions: reaction time = 72 h, ionic strength = 0.1 M $NaNO_3$ solution, a solid/solution ratio of 0.5 $g \cdot L^{-1}$ for TBir and 0.1 $g \cdot L^{-1}$ for HBir, and temperature = 25 ± 2 ^{o}C.

	Initial Cd concentraion (μM)		Cd^{2+} adsorption density ($\mu mol \cdot m^{-2}$)		Fraction of Cd adsorbed (%)	
pH	TBir	HBir	TBir	HBir	TBir	HBir
4	133.4	177.9	3.00 ± 0.10	46.39 ± 0.12	29.1 ± 1.0	68.7 ± 1.2
5	133.4	177.9	3.74 ± 0.09	50.15 ± 0.06	36.3 ± 0.9	74.2 ± 0.6
6	133.4	177.9	5.04 ± 0.03	54.16 ± 0.01	48.9 ± 0.3	80.2 ± 0.1
6.5	133.4	177.9	6.33 ± 0.01	55.50 ± 0.03	61.5 ± 0.1	82.1 ± 0.3
7	133.4	177.9	7.64 ± 0.09	57.21 ± 0.03	74.2 ± 0.9	84.7 ± 0.3
7.5	133.4	177.9	8.90 ± 0.20	60.19 ± 0.03	86.4 ± 1.9	89.1 ± 0.3
8	133.4	177.9	9.83 ± 0.01	62.36 ± 0.03	95.5 ± 0.1	92.3 ± 0.3

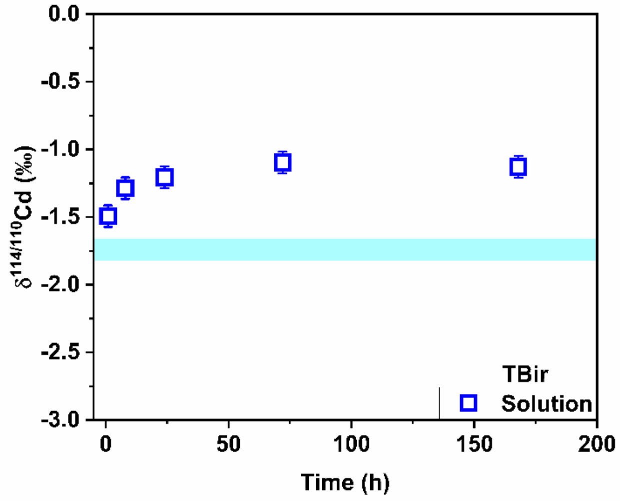

Figure S7 The kinetic evolution of aqueous Cd isotopic composition with time during adsorption onto TBir at pH 6 in 0.1 M $NaNO_3$. It showed that a kinetic isotope effect was observed in the initial reaction stage and then the isotopic equilibrium was reached at 72 h for TBir.

Table S4 Isotopic fractionation results of Cd during adsorption on TBir in kinetic and pH edge experiments.

pH	Initial Cd (μM)	Time (h)	Cd adsorbed (%)	$\delta^{114/110}Cd_{solution}$ (‰)	$\delta^{114/110}Cd_{solid}$ (‰)	Mass balance (‰)	$\Delta^{114/110}Cd_{solid\text{-}solution}$ (‰)
Adsorption kinetic experiments (ionic strength = 0.1 M $NaNO_3$ solution)							
6	133.4	1	41.7	-1.49 ± 0.08			
6	133.4	8	47.1	-1.29 ± 0.08			
6	133.4	24	50.4	-1.21 ± 0.08			
6	133.4	72	58.1	-1.10 ± 0.08			
6	133.4	168	58.2	-1.13 ± 0.08			
Adsorption edge experiments (ionic strength = 0.1 M $NaNO_3$ solution)							
4	133.4	72	28.2	-1.29 ± 0.08	-2.72 ± 0.08	-1.69 ± 0.06	-1.43 ± 0.11
5	133.4	72	35.4	-1.28 ± 0.08	-2.67 ± 0.09	-1.77 ± 0.06	-1.39 ± 0.12
6	133.4	72	48.6	-1.05 ± 0.11	-2.44 ± 0.10	-1.73 ± 0.07	-1.40 ± 0.15
7	133.4	72	73.3	-0.58 ± 0.08	-2.20 ± 0.10	-1.77 ± 0.08	-1.62 ± 0.13
8	133.4	72	95.6	-0.32 ± 0.11	-1.82 ± 0.08	-1.75 ± 0.08	-1.50 ± 0.13

Table S5 Isotopic fractionation results of Cd during adsorption on HBir in pH edge experiments.

pH	Initial Cd (μM)	Time (h)	Cd adsorbed (%)	$\delta^{114/110}Cd_{solution}$ (‰)	$\delta^{114/110}Cd_{solid}$ (‰)	Mass balance (‰)	$\Delta^{114/110}Cd_{solid\text{-}solution}$ (‰)
Adsorption edge experiments (IS=0.1 M $NaNO_3$ solution)							
4	177.9	72	59.4	-1.19 ± 0.08	-2.12 ± 0.08	-1.74 ± 0.06	-0.92 ± 0.11
5	177.9	72	66.2	-1.15 ± 0.08	-1.98 ± 0.08	-1.70 ± 0.06	-0.83 ± 0.11
6	177.9	72	73.6	-1.08 ± 0.08	-1.94 ± 0.08	-1.71 ± 0.06	-0.86 ± 0.11
7	177.9	72	79.9	-1.00 ± 0.08	-1.90 ± 0.08	-1.72 ± 0.07	-0.90 ± 0.11
8	177.9	72	90.0	-0.91 ± 0.09	-1.78 ± 0.08	-1.70 ± 0.07	-0.87 ± 0.12

Table S6 Fitting results of Cd K-edge EXAFS spectra for aqueous $Cd(NO_3)_2$ standard and typical Cd adsorbed samples, without a third cumulant (Cum.) for TBir and HBir in the first Cd−O shell fitting. ($S_0^2 = 0.95$)[6]

Sample	Path	CN	R (Å)	σ^2 (Å^2)	ΔE (eV)	Reduced χ^2	χ^2	R-factor
$Cd(NO_3)_{2,\ aq}$	Cd-O	7.8 ± 0.4	2.27 ± 0.01	0.0101 ± 0.0009	3.2 ± 0.6	495.22	4821.20	0.0064
HBir	Cd-O	8.4 ± 0.8	2.24 ± 0.01	0.0116 ± 0.0017	1.4 ± 1.0	3.75	19.42	0.0067
	Cd-Mn	10.4 ± 3.0	3.62 ± 0.01	0.0145 ± 0.0031				
TBir	Cd-O	5.9 ± 1.0	2.23 ± 0.01	0.0002 ± 0.0018	-1.0 ± 1.8	1.65	12.77	0.0441
	Cd-Mn	2.4 ± 1.0	3.64 ± 0.03	0.0030[a]				

[a] This parameter was fixed during the fitting.

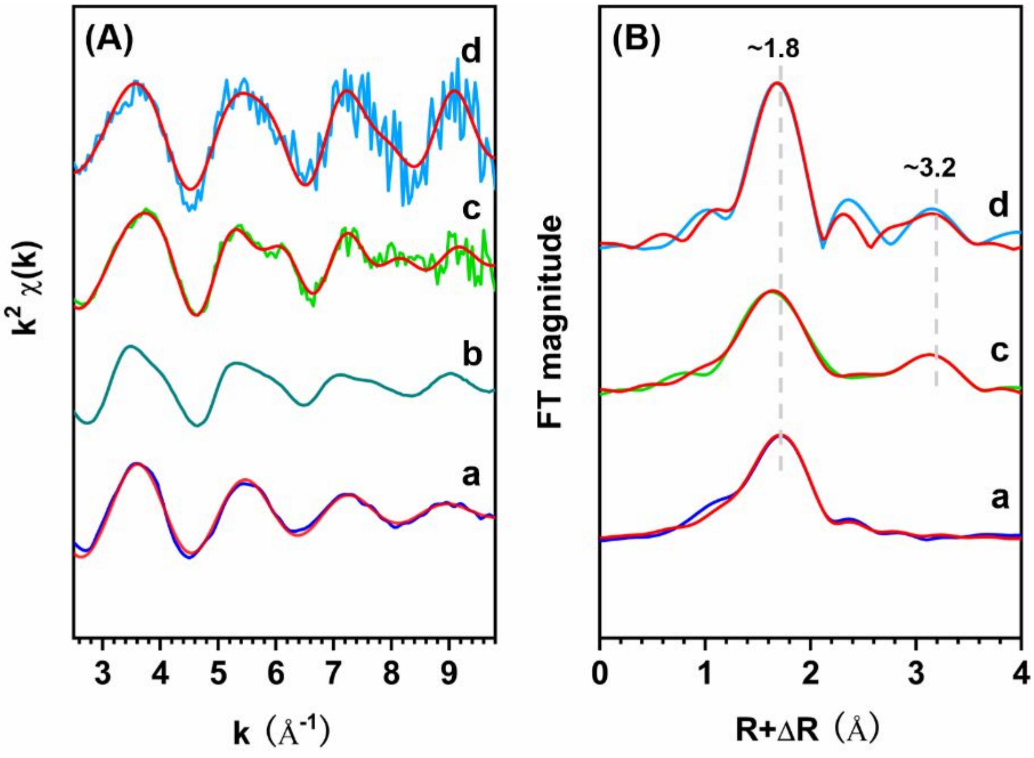

Figure S8 The k^2-weighted Cd K-edge EXAFS (A) and the corresponding Fourier transformed spectra (FTs, B) of aqueous $Cd(NO_3)_2$ (a), $Cd(OH)_2$ (b), and Cd-adsorbed samples HBir (c) and TBir (d), overlaid with the best fits without a third cumulant for HBir and TBir in the first Cd-O shell fitting. The experimental data and the best fits are showed as colored and red lines respectively.

Table S7 Experimental and modeling proportions of Cd adsorbed onto HBir edge sites and vacancies over a pH range of 4-8. Experimental conditions: reaction time = 72 h, ionic strength = 0.1 M $NaNO_3$ solution, a solid/solution ratio of 0.1 $g \cdot L^{-1}$ for HBir, and temperature = 25 ± 2 ^{o}C.

pH	Cd adsorbed (%)			
	experimental	modeling		
		total	edge sites	vacancies
4 ± 0.05	68.7 ± 1.2	59	0	59
5 ± 0.05	74.2 ± 0.6	65	0	65
6 ± 0.05	80.2 ± 0.1	71	7	64
7 ± 0.05	84.7 ± 0.3	90	30	60
8 ± 0.05	92.3 ± 0.3	96	39	57

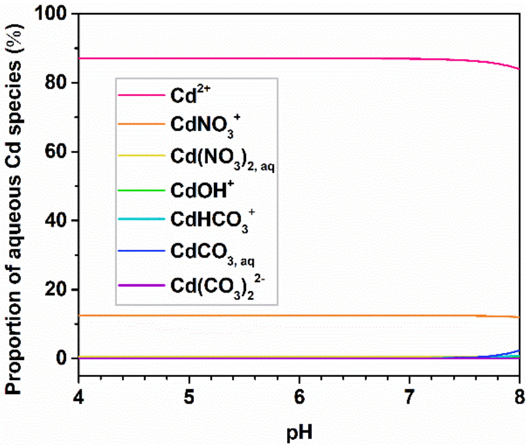

Figure S9 Changes of aqueous Cd species as a function of pH calculated using Visual MINTEQ 3.1 for 177.9 μM $Cd(NO_3)_2$ in 0.1 M $NaNO_3$ solution[7].

Text S3 Mineral transformation of TBir after acidification at pH4.

Powder XRD pattern of TBir after acidification at pH4 for 72 h (TBir_pH4_72h) shows different diffraction peaks from that of the original TBir (Figure S10), and resembles that of the transformation product of Na-rich birnessite by acidifying at pH4 in our previous study (hereafter referred as NaBu_pH4)[8]. NaBu_pH4 layers are composed of 60% 1H phase (one-layer hexagonal structural model) and 40% 1M phase (one-layer monoclinic model).

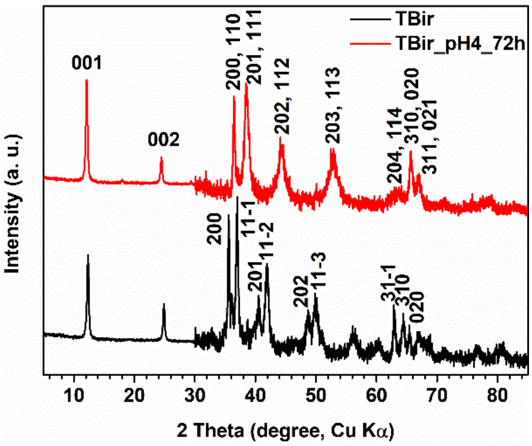

Figure S10 Powder XRD patterns of TBir before and after acidification at pH4 for 72 h. The intensity in the high-angle region (30–85 °2θ) was scaled by a factor of 10 for clarity.

References

1. Lanson, B.; Marcus, M. A.; Fakra, S.; Panfili, F.; Geoffroy, N.; Manceau, A., Formation of Zn–Ca phyllomanganate nanoparticles in grass roots. *Geochim. Cosmochim. Acta* **2008,** *72*, (10), 2478-2490.
2. Grangeon, S.; Manceau, A.; Guilhermet, J.; Gaillot, A.; Lanson, M.; Lanson, B., Zn sorption modifies dynamically the layer and interlayer structure of vernadite. *Geochim. Cosmochim. Acta* **2012,** *85*, 302-313.
3. Grangeon, S.; Lanson, B.; Miyata, N.; Tani, Y.; Manceau, A., Structure of nanocrystalline phyllomanganates produced by freshwater fungi. *Am. Mineral.* **2010,** *95*, (11-12), 1608-1616.
4. Gaillot, A.-C.; Flot, D.; Drits, V. A.; Manceau, A.; Burghammer, M.; Lanson, B., Structure of Synthetic K-rich Birnessite Obtained by High-Temperature Decomposition of KMnO4. I. Two-Layer Polytype from 800 °C Experiment. *Chem. Mater.* **2003,** *15*, (24), 4666-4678.
5. Gaillot, A.-C.; Drits, V. A.; Manceau, A.; Lanson, B., Structure of the synthetic K-rich phyllomanganate birnessite obtained by high-temperature decomposition of KMnO4. *Microporous Mesoporous Mater.* **2007,** *98*, (1-3), 267-282.
6. Sun, Q.; Cui, P. X.; Zhu, M.; Fan, T. T.; Ata-Ul-Karim, S. T.; Gu, J. H.; Wu, S.; Zhou, D. M.; Wang, Y. J., Cd(II) retention and remobilization on δ-MnO2 and Mn(III)-rich δ-MnO2 affected by Mn(II). *Environ. Int.* **2019,** *130*, 104932.
7. Gustafsson, J., Visual MINTEQ 3.1, KTH Royal Institute of Technology. *Dept of*

Land and Water Resource Engineering, Stockholm **2014**.

8. Lanson, B.; Drits, V. A.; Silvester, E.; Manceau, A., Structure of H-exchanged hexagonal birnessite and its mechanism of formation from Na-rich monoclinic buserite at low pH. *Am. Mineral.* **2000,** *85*, (5-6), 826-838.